ACS OMEGA

http://pubs.acs.org/journal/acsodf
Article

Numerical Simulation of Biochar Substitution for Sintering Process Combining Coarse Particle Size and Selective Oxygen Enrichment

Zecheng Wang, Jin Cai,* Xiangwei Kong,* Mingzhu Yu, Liang Zhao, Chunwen Yan, Ailing Liu, and Hao Wu

Cite This: https://doi.org/10.1021/acsomega.6c00999
Read Online

ABSTRACT: For the green production of iron ore sintering processes, the high-proportion use of biomass energy faces the problem of severe deterioration in sintering quality and high comprehensive usage cost. This study proposes the use of medium- and low-grade biochar and their coarse particle size combined with selective oxygen enrichment at the inlet of the sintering bed for continuous quality improvement and comprehensive usage cost reduction. First, by considering submodels such as the heat supply from the dual-fuel phases of coke and biochar, as well as their pyrolysis, volatile combustion, char combustion, and gasification, NO generation and reduction, a numerical model of the sintering process under biochar substitution was established. Then, the application effect of biochar under different process operation modes was studied through numerical simulation. The results show that the method of using a coarsened particle size can enhance various thermal indicators of sintering. When the biochar particle size is in the range of 1.6 mm to 4.8 mm and under a 60% substitution rate, the yield can reach 45%. However, an excessively coarse particle size of biochar will cause incomplete combustion that gradually expands in the longitudinal depth of the sintering bed. The selective oxygen enrichment and segregation process (case 21) increased the combustion rate of solid fuels. The maximum combustion rates of coke and biochar in the near-inlet area of the bed (at 300s) were 81.95 mol/m^3 s and 48.50 mol/m^3 s, respectively. Compared with the combustion rates of coke and biochar in the case without oxygen enrichment (case 10:42.36 and 24.77 mol/m^3 s), they increased by 93.46% and 95.80%, respectively. Fuel utilization efficiency and energy release were effectively improved, strengthening the thermal curves of the sintering process.

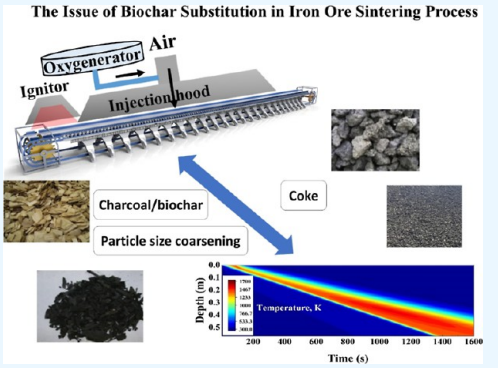

1. INTRODUCTION

Iron and steel industry is one of the most energy- and carbon-intensive industries. Its main energy sources are coal and coke. The energy consumption of iron and steel accounts for approximately 15% to 20% of global industrial energy consumption, and carbon dioxide emissions account for about 5% to 7% of the global total.[1] Iron ore sintering is an important operational unit in iron and steel enterprises, being the primary source of blast furnace raw materials. Its energy consumption accounts for about 20% of that of the steel plant and is severely polluted.[2,3] As China took the lead in proposing the goals of achieving a carbon peak by 2030 and carbon emission reduction by 2050, green and clean production in all processes of the iron and steel industry has become an important strategic development direction. Biomass-based fuels have gradually attracted the interest of many metallurgists due to their characteristics such as carbon neutrality and low sulfur and nitrogen contents.[4,5] Currently, many research results support the view that charcoal has no technical obstacles in iron ore sintering and is superior to coke. Considering environmental and sustainable development aspects, the transition from fossil fuels to charcoal obviously has great potential.[6] However, due to the high volatile content of biomass-based fuels and the excessively fast combustion reaction rate, their application in sintering production faces problems such as a serious decline in sintering quality, low substitution rate, and high comprehensive usage cost, which have not been effectively solved.

According to previous studies, modifying materials using heat treatment technology can improve fuel performance, and surface coating technology can also overcome some of the negative impacts caused by the increased reactivity of fuels. Fan et al.[7,8] evaluated the characteristics of four types of straw-based fuels, including raw straw (RS), preformed straw (PS), straw char (SC), and PS char (PSC). PSC ingeniously integrated the advantages of PS and SC by a joint preformation−carbonization

Received: February 9, 2026
Revised: May 10, 2026
Accepted: May 15, 2026

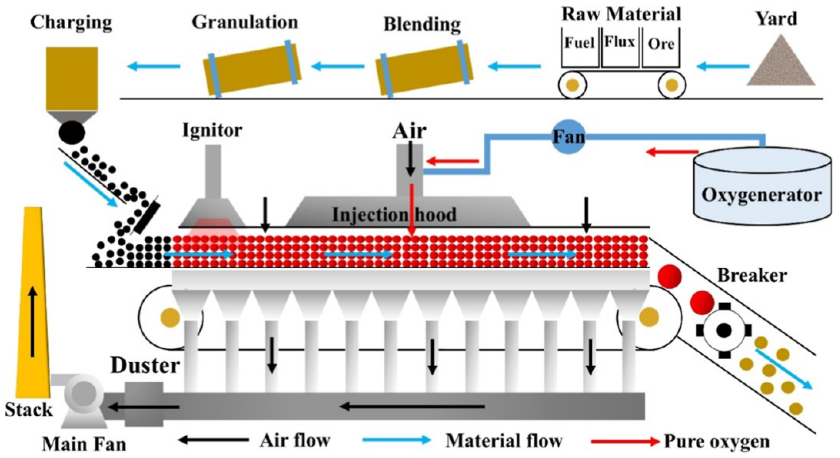

Figure 1. Typical iron ore sintering process.

process. Comparable sintering performance was achieved when improving the replacement percentage of PSC to coke breeze to 40%, and its capacity for reducing CO2, SOx, and NOx emissions achieved 24.5%, 26.6%, and 28.2%, respectively. Gul et al.[9] agglomerated charcoal with pyrolysis oil and reheated it at high temperatures to make the obtained biochar have sufficient hardness, appropriate porosity, and reactivity. Currently, the preparation process of high-grade biochar that meets the needs of metallurgical fuel processes still needs continuous optimization to significantly reduce its costs. This is also the main crux of the inability of biochar substitution technology to move toward industrial sintering production.[10] Zhao et al.[11] developed a combustion model of fuel particles adhered to fine-grained ore and flux, as well as a two-dimensional sintering model. They found that merely matching the overall combustion rate may not guarantee the comparability of sintering performance; it is necessary to ensure that the apparent density and water-holding capacity of the alternative fuel are close to those of coke to ensure the similarity of the granulation performance. If these conditions are not fully met, then the combustion efficiency, the characteristics of the formed flame front (such as width, temperature, and speed), and the sintering performance will all decrease. Obviously, the coating structure can be diverse and can inhibit the high reactivity of the fuel to a certain extent, but this also increases the process complexity and difficulty of production operations. Generally, a separate coating device is required for fuel pretreatment, and controlling the thickness of the coating layer is also a key challenge.

How to achieve the high-proportion substitution rate of low-grade biochar without adding additional equipment, processes, and operating conditions is obviously an important direction to solve the problem. Researchers ever attempted to use coarse wood charcoal to reduce the reactivity of the fuel, which also had a positive effect, providing us with new insights. Kawaguchi and Hara[12] conducted sintering experiments using biochar and pointed out that it is necessary to optimize operations such as size control and moisture control of biochar because its combustion rate is too high. Gan et al.[13] precisely controlled the combustion rate by coarsening the particle size. The maximum temperature and high-temperature holding time of sintering can be increased and prolonged. Cheng Zhilong et al.[14,15] experimentally tested the effects of three improving measures (proposing the equivalent fixed carbon substitution approach, increasing charcoal particle size, and adopting coated charcoal combustion). With the help of an equivalent fixed carbon substitution approach, coarse charcoal, and coated charcoal particles, the peak temperature (PT), holding time above 1100 °C, melting quantity index (MQI), and combustion efficiency were increased in the charcoal sintering process. Given the economic considerations of minimizing additional energy input and reducing costs, fully utilizing the inherent properties of biomass fuels should be the first step in solving the problem. Therefore, studying low-grade biochar with a wide range of industrial sources and relatively low costs (volatile matter content of about 20%−30%), combined with their particle size coarsening, has great significance in sintering.

In addition to the single process of coarsening particle size, the study of multiprocess combinations also provides certain conditions for further reducing the process cost of biochar.[16−18] Cheng et al.[19] jointly injected oxygen-enriched gas and methane into the area near the inlet of the sintering bed, which improved the thermal state and sintering performance of the sintered surface layer. Similar good effects were also described in the study by Ni et al.,[20] but they also found that excessive oxygen enrichment was not beneficial to either the sintering yield or the sintering quality. In addition, increasing the oxygen concentration will increase NO_x emissions. Castro et al.,[21,22] Cai et al.,[23,24] and others have, respectively, used comprehensive mathematical models of transport phenomena to study scenarios combining biochar and hydrogen-rich injection processes. The results show that this process combination overcomes the problem of insufficient heat supply at the combustion front during biochar sintering. A good temperature distribution promotes the formation of calcium ferrites of structural shape, endowing the sinter with sufficient metallurgical properties. These works indicate that multiprocess combination and numerical simulation may become an effective method and tool for researching biomass-based fuel substitution. Considering that existing and newly built sintering machines are equipped with hydrogen-rich and oxygen-rich devices, and the process mode and equipment operating conditions are relatively mature, these processes should be combined and used with low-grade and medium-grade biochar, coarsening particle size, etc. to further continuously reduce the application cost of biochar and improve the quality of sintering.

On the basis of previous studies, to fully utilize the potential of the inherent properties of biochar, minimize additional energy supply to the greatest extent, reduce the comprehensive cost of applying biochar in sintering, and improve sintering quality and reduce comprehensive usage costs, this study proposes the

https://doi.org/10.1021/acsomega.6c00999
ACS Omega XXXX, XXX, XXX−XXX

combination of using low-grade and medium-grade biochar, coarse-grained biochar, and selective oxygen enrichment at the sintering bed inlet to achieve a quality improvement. First, a mathematical model for low-carbon sintering of iron ore under biochar replacement was established. This model can couple heat and mass transfer with a nitrogen oxide emission submodel, enabling simultaneous evaluation of thermal performance and minimization of nitrogen oxide emissions. Second, multiple thermal index parameters were selected to discuss the impact of the combined process of coarsened particle size and selective oxygen enrichment on the sintering quality and NO emissions of iron ore sintering, and an in-depth explanation of the mechanism of process enhancement was provided. Finally, preliminary use of selective hydrogen-rich injection, selective oxygen enrichment, and coarsening particle size was initially used to achieve the level of full coke sintering for 60% biochar. The research methods and results provide technical support for improving the sintering quality under the replacement of biochar and further reducing its comprehensive use cost.

2. MODEL ESTABLISHMENT

2.1. Model Introduction

2.1.1. Process Introduction. In the iron ore sintering process, as shown in Figure 1, first, raw materials, such as iron ore, fluxes, and fuel, are mixed. The fully mixed mixture is further granulated in a drum, and water is added to form moist pseudoparticles. Charging devices such as roller conveyors are employed to arrange the mixture onto the sintering pallet. The pallet loaded with the mixture slowly moves from left to right and then enters into the ignition hood. The combustion process starts, and the fuel particles on the surface of the sinter bed are first ignited. The flame front moves downward from the surface of the bed to the bottom of the pellet. Air is drawn through a suction fan to create negative pressure to sustain combustion, ultimately forming a sinter that meets the requirements of the blast furnace.

In this study, oxygen-enriched gas injection starts after the ignition process and covers the partial sintering time (ST) (mainly in the area near the entrance of the sintering bed). On the basis of literature research, the use of processes such as coarsened particle size and oxygen-enriched injection during the sintering process of medium- and low-grade biochar may bring good results, which is the research focus of this numerical simulation.

2.1.2. Model Assumptions. The core goal of modeling is the sinter mixture carried by the trolley section, namely, the sinter bed. In research focusing on chemical reaction mechanisms, heat and mass transfer processes, etc., sinter bed models are still mainly one- and two-dimensional. The main assumptions and simplifications adopted are as follows.

This system is a 1D transient process. When the transfer phenomena along the length and width directions of the sintering machine can be neglected, the 1D and 2D representations are equivalent, which mathematically describe the sintering process, as shown in Figure 2. The analysis considers the entire sintering bed as a porous zone. Gas and solid phases are independent and have different temperatures. The solid-phase components considered in the model include moisture, melt, coke, biomass fuel, limestone, dolomite, slaked lime, hematite (Fe_2O_3), magnetite (Fe_3O_4), wüstite (FeO), and 6 pyrolysis pseudocomponents. The gas-phase components include CO, CO_2, H_2O, O_2, H_2, CH_4, two types of tar

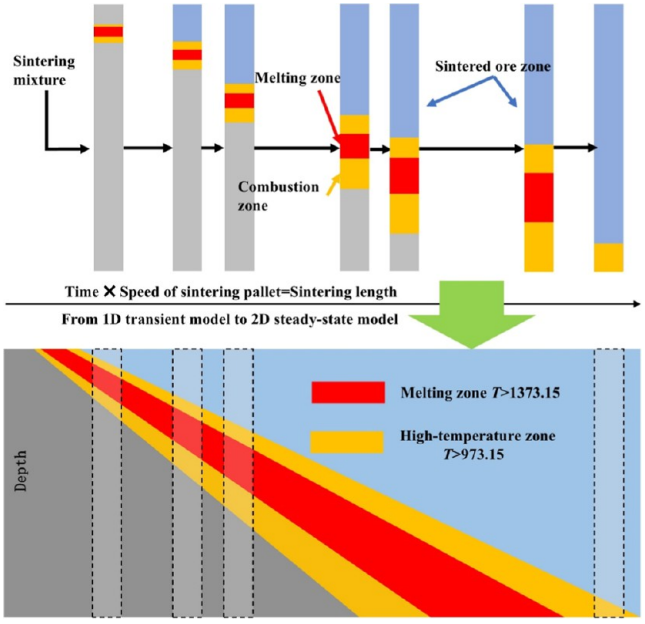

Figure 2. Extension of the 1D transient model to the 2D steady model of the sintering bed.

($C_{0.83}H_{2.3}O_{1.07}$ and $C_{1.44}H_{3.6}O_{0.52}$), HCN, NO, and inert gas N_2. Due to the relatively high volatile content of biochar, it is necessary to consider the pyrolysis release process. In the expression for pore space reorganization, factors such as bed shrinkage, shape factor, and char burnout are considered.

2.1.3. Model Structure. The overall structure of the proposed model is shown in Figure 3 and is integrated into commercial CFD software. The submodels will be compiled into UDFs and coupled into the system of governing equations. The process of iron ore sintering, combined with biochar substitution, coarse particle size, and selective oxygen enrichment, is simulated by considering a wide range of physical and chemical mechanisms.

2.2. Governing Equations

Based on the above assumptions and the overall structure of the model, the governing equations describing heat and mass transfer as well as flow during sintering can be listed, namely the gas−solid phase mass and component conservation equations, the gas−solid phase energy conservation equation, the gas-phase momentum conservation equation, and the ideal gas-state equation. These are used to solve for the distribution of mass, velocity, temperature, and pressure of gas-phase components in the bed.[25,26]

(1) Gas-phase mass conservation equation:

$$\frac{\partial(\varepsilon\rho_g)}{\partial t} + \nabla\cdot(\varepsilon\rho_g \boldsymbol{u}) = \sum_k M_k R_k \quad (1)$$

In the formula, $\boldsymbol{u}$ is the vector form of gas velocity, in m/s; ε is the porosity of the sintering bed; ρ_g is the density of the mixed gas, in kg/m^3; t is time, in s; k is the chemical reaction index, where k = 1−32; M_k is the molar mass of reaction k, in kg/mol; R_k is the chemical reaction rate of reaction k, in mol/(m^3·s); $\sum_k M_k R_k$ is the mass source term, representing the rate of all chemical reactions, in kg/(m^3·s).

(2) Solid-phase mass conservation equation:

https://doi.org/10.1021/acsomega.6c00999
ACS Omega XXXX, XXX, XXX−XXX

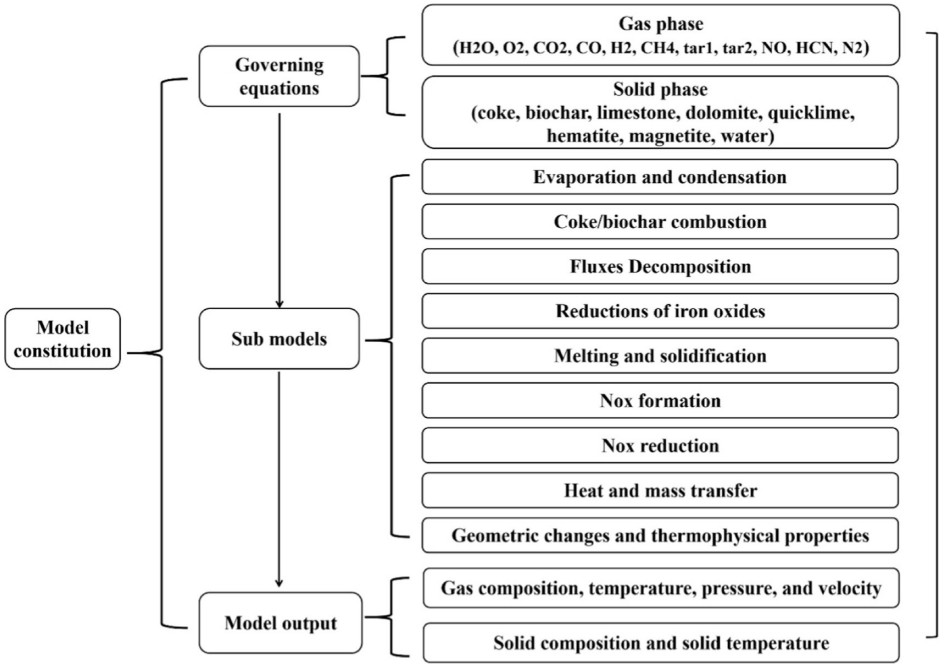

Figure 3. Overall structure of the model.

$$\frac{\partial((1-\varepsilon)\rho_s)}{\partial t} = -\sum_k M_k R_k \tag{2}$$

In the formula, ρ_s is the density of the solid mixture, in kg/m^3; $\rho_s(1\text{-}\varepsilon)$ is the bulk density of the sintered material layer, in kg/m^3.

(3) Conservation equation of gas-phase components:

$$\frac{\partial(\varepsilon\rho_g Y_i)}{\partial t} + \nabla\cdot(\varepsilon\rho_g Y_i \boldsymbol{u}) = \sum_k \sum_i M_{i,k} R_{i,k} \tag{3}$$

In the formula, Y_i is the mass fraction of the gas-phase component i; i is the index of the gas-phase component; $M_{i,k}$ is the molar mass of the gas-phase component i in the reaction, in kg/mol. $\sum_k\sum_i M_{i,k}R_{i,k}$ is the source term of the gas-phase component, representing the generation rate of the gas-phase component i in all chemical reactions, in kg/(m^3·s).

(4) Conservation equation of solid-phase components:

$$\frac{\partial((1-\varepsilon)\rho_s w_j)}{\partial t} = -\sum_k \sum_j M_{j,k} R_{j,k} \tag{4}$$

In the formula, w_j is the mass fraction of the solid-phase component j; $M_{j,k}$ is the molar mass of the solid-phase component j in the reaction, in kg/mol. $-\sum_k\sum_j M_{j,k}R_{j,k}$ is the source term of the solid-phase component, which represents the generation rate of the solid-phase component j in all chemical reactions, in kg/(m^3·s).

(5) Gas-phase energy conservation equation:

$$\frac{\partial}{\partial t}(\varepsilon\rho_g c_{p,g} T_g) + \nabla\cdot(\varepsilon\rho_g c_{p,g}\boldsymbol{u} T_g) = \nabla\cdot(\varepsilon\lambda_g \nabla T_g) + hA_{sa}(T_s - T_g) + \sum_k\sum_i (1-\varphi) M_{i,k} R_{i,k} \Delta H_{i,k} \tag{5}$$

In the formula, $c_{p,g}$ is the specific heat of the gas mixture, in J/(kg·K); T_g and T_s are the temperatures of the gas-phase and solid-phase mixtures, respectively, in K; λ_g is the thermal conductivity of the gas phase, in W/(m·K); h is the convective heat transfer coefficient, in W/(m^2·K); A_{sa} is the specific surface area of the solid particles, in m^2/m^3; $hA_{sa}(T_s\text{-}T_g)$ and $\sum_k\sum_i(1\text{-}\varphi)M_{i,k}R_{i,k}\Delta H_{i,k}$ are the gas energy source terms, representing the convective heat transfer between gas and solid and the part of all chemical reaction heat acting on the gas phase, respectively, in J/(mol·K).

(6) Solid-phase energy conservation equation:

$$\frac{\partial}{\partial t}((1-\varepsilon)\rho_s c_{p,s} T_s) + \nabla\cdot(\varepsilon\rho_s c_{p,s}\boldsymbol{u} T_s) = \nabla\cdot((1-\varepsilon)\lambda_{s,\mathrm{eff}}\nabla T_s) + hA_{sa}(T_g - T_s) + \sum_k\sum_j \varphi M_{j,k} R_{j,k} \Delta H_{j,k} \tag{6}$$

In the formula, $c_{p,s}$ is the specific heat capacity of the solid mixture, in J/(kg·K); $\lambda_{s,\mathrm{eff}}$ is the effective thermal conductivity of the solid phase, in W/m·K; $hA_{sa}(T_g\text{-}T_s)$ and $\sum_k\sum_j\varphi M_{j,k}R_{j,k}\Delta H_{j,k}$ are the solid energy source terms, representing the gas−solid convective heat transfer and the part of all chemical reaction heat acting on the solid phase, respectively, in J/(mol·K).

(7) Momentum conservation equation of the gas phase:

$$\frac{\partial(\varepsilon\rho_g \boldsymbol{u})}{\partial t} + \nabla\cdot(\varepsilon\rho_g \boldsymbol{u}\boldsymbol{u}) = \nabla\cdot(\mu\nabla\boldsymbol{u}) - \nabla P_g - \mathrm{Source_M} \tag{7}$$

$$\mathrm{Source_M} = \frac{3.5(1-\varepsilon)}{\varepsilon^3 \varsigma d_p}\cdot\rho_g\cdot|\boldsymbol{u}|\boldsymbol{u} + \frac{150(1-\varepsilon)^2}{\varepsilon^3(\varsigma d_p)^2}\cdot\mu\cdot\boldsymbol{u} \tag{8}$$

In the formula, P_g is the gas-phase pressure, Pa; $\mathrm{Source_M}$ is the gas momentum source term.

The Reynolds number Re of the sintering process is between 100 and 200. The flow of gas through the sinter bed has mixed

https://doi.org/10.1021/acsomega.6c00999
ACS Omega XXXX, XXX, XXX−XXX

Table 1. Chemical Reaction and Reaction Rate

submodel	reaction rate	equation no
1. Evaporation and condensation		
$H_2O(l) \leftrightarrow H_2O(g)$	$R_{H_2O} = \begin{cases} \chi \frac{k_{m,H_2O} A_{sa}}{R_g T_g}(P_{sat} - P_{H_2O}), \text{ When } P_{sat} > P_{H_2O} \\ \frac{k_{m,H_2O} A_{sa}}{R_g T_g}(P_{sat} - P_{H_2O}), \text{ When } P_{sat} < P_{H_2O} \end{cases}$ (10)	10[30,31]
2. Coke/biochar combustion		
2a. Pyrolysis reaction solid fuel j $\begin{cases} \rightarrow \text{light gases}_j \\ \rightarrow \text{tar}_j \\ \rightarrow \text{char}_j \end{cases}$ (j = coke, biochar)	solid fuel j: $R_{vol,i} = k_{vol,i} \cdot m_{vol,j}$ (11) (i = gas, tar, char; j = coke, biochar)	11[32]
2b. Volatiles combustion and homogeneous reactions		
$C_{0.83}H_{2.3}O_{1.07} + 0.45O_2 \rightarrow 0.83CO + 1.15\ H_2O$	$59.8 T_g P^{0.3} C_{tar}^{0.5} C_{O_2} \exp(-12200/T_g)$ (12)	12[33,34]
$C_{1.44}H_{3.6}O_{0.52} + 1.36O_2 \rightarrow 1.44CO + 1.80\ H_2O$	$59.8 T_g P^{0.3} C_{tar}^{0.5} C_{O_2} \exp(-12200/T_g)$ (13)	13[33,34]
$CO + 0.5O_2 \rightarrow CO_2$	$3.25 \times 10^7 C_{O_2}^{0.5} C_{H_2O}^{0.5} C_{CO} \exp(-15098/T_g)$ (14)	14[35]
$CH_4 + 1.5O_2 \rightarrow CO + 2H_2O$	$1.6 \times 10^{10} C_{CH_4}^{0.7} C_{O_2}^{0.8} \exp(-24157/T_g)$ (15)	15[35]
$H_2 + 0.5O_2 \rightarrow H_2O$	$51.8 \times C_{H_2}^{1.5} C_{O_2} T_g^{1.5} \exp(-3420/T_g)$ (16)	16[35]
$CO_2 \rightarrow CO + 0.5O_2$	$7.5 \times 10^{11} C_{CO2} \exp(-46500/T_g)$ (17)	17[26]
$CO + H_2O \rightarrow H_2 + CO_2$	$2.78 \times C_{H_2O} C_{CO} \exp(-1510/T_g)$ (18)	18[36]
$H_2 + CO_2 \rightarrow CO + H_2O$	$93.96 \times C_{CO_2} C_{H_2} \exp(-5604/T_g)$ (19)	19[26]
2c. Char combustion and gasification		
$\Omega_c C + O_2 \rightarrow 2(\Omega_c - 1)CO + (2 - \Omega_c)CO_2$ $\Omega_c = \frac{2(1 + 4.3\exp(-3390/T_s))}{(2 + 4.3\exp(-3390/T_s))}$	solid fuel j: $R_{char,i} = \frac{4\pi r_{char0,j}^2 n_j C_i}{\frac{1}{k_{m,i}} + \frac{r_{char0,j}(r_{char0,j} - r_{char,j})}{D_{i,eff} r_{char,j}} + \frac{1}{k_{char,i}}\left(\frac{r_{char0,j}}{r_{char,j}}\right)^2}$ (20) (i = O_2, CO_2, H_2O, H_2; j = coke, biochar)	20[35,37−39]
	$k_{m,o_2} = 1.715\exp(-9000/T_s)$	
$C + CO_2 \rightarrow 2CO$	$k_{m,CO_2} = 3.42\exp(-15600/T_s)$	
$C + H_2O \rightarrow CO + H_2$	$k_{m,H_2O} = 3.42\exp(-15600/T_s)$	
$C + 2H_2 \rightarrow CH_4$	$k_{m,H_2} = 3.42 \times 10^{-3}\exp(-15600/T_s)$	
3. Fluxes Decomposition		
3a. Decomposition of limestone $CaCO_3 \rightarrow CaO + CO_2$	$R_{ls} = \frac{4\pi r_{ls0}^2 n_{ls}(C_{CO_2}^* - C_{CO_2})}{\frac{1}{k_{m,CO_2}} + \frac{r_{ls0}(r_{ls0} - r_{ls})}{D_{CO_2,eff} r_{ls}} + \frac{1}{k_{ls}}\left(\frac{r_{ls0}}{r_{ls}}\right)^2}$ (21)	21[40,41]
3b. Decomposition of dolomite $CaMg(CO_3)_2 \rightarrow CaO + MgO + 2CO_2$	$\frac{dX_{dl}}{dt} = 1.628 \times 10^7 \exp(7.21165 - 9959.45/T_s) \cdot (1 - X_{dl})^{0.4043}$ (22)	22[42]
3c. Decomposition of hydrated lime $Ca(OH)_2 \rightarrow CaO + H_2O$	$\frac{dX_{hl}}{dt} = (2.932 + 3.151 \cdot X_{hl}) \times 10^5 \exp(-113592.0/RT_s)(1 - X_{hl})^{0.77}$ (23)	23[43]
4. Reductions of iron oxides		
$3Fe_2O_3 + CO/H_2 \rightarrow 2Fe_3O_4 + CO_2/H_2O$	$R_{n,CO} = 4\pi r_{ore0}^2 \frac{\rho_g}{W_{CO}} \sum_{m=1}^{3} \alpha_{n,m}\left[K_{m,CO}\frac{Y_{CO}}{M_{CO}} - \frac{Y_{CO_2}}{M_{CO_2}}\right]$ (24)	24[44−46]
$Fe_3O_4 + CO/H_2 \rightarrow 3FeO + CO_2/H_2O$	$R_{n,H_2} = 4\pi r_{ore0}^2 \frac{\rho_g}{W_{H_2}} \sum_{m=1}^{3} \alpha_{n,m}\left[K_{m,H_2}\frac{Y_{CO}}{M_{CO}} - \frac{Y_{CO_2}}{M_{CO_2}}\right]$ (25)	25[44−46]
$FeO + CO/H_2 \rightarrow Fe + CO_2/H_2O$		

https://doi.org/10.1021/acsomega.6c00999
ACS Omega XXXX, XXX, XXX−XXX

Table 1. continued

submodel	reaction rate	equation no
	5. Melting and solidification	
Raw mixture → Melting → Sintered ore	$M_f = \begin{cases} 1 & (T_s > T_{max}) \\ \left(\frac{T_s - T_m}{T_{max} - T_m}\right)^{\theta}, & (T_m \le T_s \le T_{max}) \\ 0 & (T_s < T_m) \end{cases}$ (26)	26[46,48]
6. Nox formation		
	6a. Formation of fuel-type NO from volatiles (Volatile-N)	
solid fuel$j$: Volatile-N → HCN (j = coke, biochar)	$R_{HCN,j} = R_{vol,j} w_{vol-N,j} M_{HCN}/M_N$ (27) (j = coke, biochar)	27[49−53]
$HCN + O_2 \rightarrow NO + \cdots$	$R_{HCN1} = \frac{\rho_g \cdot 1000}{M_{mix}} 1.0 \times 10^6 X_{HCN} X_{O_2}^f \exp(-280300.0/RT_g)$ (28)	28[49−53]
$HCN + NO \rightarrow N_2 + \cdots$	$R_{HCN2} = \frac{\rho_g \cdot 1000}{M_{mix}} 3.0 \times 10^{12} X_{HCN} X_{NO} \exp(-251000.0/RT_g)$ (29)	29[49−53]
	6b. Fuel-type NO formation from carbon particles (Char-N)	
solid fuel$j$: Char-N + O_2→NO (j = coke, biochar)	$R_{char-N,j} = R_{char,j} \eta_{b,j} w_{char-N,j} \delta M_{NO}/M_N$ (30) (j = coke, biochar)	30[54−58]
	6c. Thermal NO formation path	
Thermal path: $N_2 + O \leftrightarrow NO + N$; $N + O_2 \leftrightarrow NO + O$; $N + OH \leftrightarrow NO + H$	$R_{NOt} = 3.0 \times 10^5 C_{O_2}^{0.5} C_{N_2} \exp(-542000/RT_g)$ (31)	31[52,55,56]
	6d. Prompt NO formation pathway	
Prompt path → NO	$R_{NOp} = M_{NO} \cdot \left(\frac{P_g}{RT_g}\right) \cdot 1.2 \times 10^7 X_{O_2}^f X_{N_2} X_{CH_4} \exp(-251200/RT_g)$ (32)	32[49,59,60]
	7. Nox reduction	
solid fuel j: C + NO → 0.5N_2 + CO(j = coke, biochar)	$R_{NOchar,j} = k_{NOchar} A_{isa,j} P_{NO} \eta_{r,j}$ (33) (j = coke, biochar)	33[55,61−63]
NO + CO → 0.5N_2 + CO_2	$R_{NO,CO} = M_{NO} \cdot 9.92 \times 10^5 C_{CO} C_{NO} \exp(-10000/T_g)$ (34)	34
8. Geometric changes	$f_s = M_f \cdot f_{s,max}$ (35)	35[64,65]
	$d_p = d_{p,ini} + M_f(d_{p,fin} - d_{p,ini})$	
	$\varsigma = \varsigma_{ini} + M_f(\varsigma_{fin} - \varsigma_{ini})$	
	$\varepsilon = \varepsilon_0 + \left(\frac{\varsigma_{ini} - \varsigma}{\varsigma_{ini} - 0.07} + \frac{f_s}{1 - f_s}\right)(1 - \varepsilon_0) + \sum n_j \frac{4\pi}{3}(r_{char0,j}^3 - r_{char,j}^3)(j$ = coke, biochar)	

characteristics of laminar and turbulent flows, which will generate viscous and inertial resistances. Therefore, the momentum eq 7 requires additional source terms to describe and calculate these two resistances. The Ergun[27−29] equation is used for calculating $Source_M$. The viscous loss term $\frac{150(1-\varepsilon)^2}{\varepsilon^3(\varsigma d_p)^2} \cdot \mu \cdot \boldsymbol{u}$ and inertial loss term are functions of the average particle size d_p, bed porosity ε, and shape factor ς.

(8) Equation of state for gases:

$$P_g = \left(\sum_i \rho_g Y_i/M_i\right) \cdot RT_g \quad (9)$$

In the formula, M_i is the molar mass of the gas-phase component i, in kg/mol; R is the universal gas constant, 8.314 J/(mol·K).

2.3. Key Submodels

In the author's previous research,[23,24] a series of submodels for the sintering process under biochar substitution have been proposed, as shown in Table 1. This study also considered changes in physical parameters such as specific heat capacity, density, viscosity, and thermal conductivity. Table 2 presents empirical formulas for thermophysical parameters.

3. SINTERING CUP EXPERIMENT AND VERIFICATION

This paper uses the experimental data from Yang et al.[67,68] to verify the proposed model during the traditional sintering process using only coke as fuel.[26,69−71] The biochar sintering data from the Fan and Gan research groups were simultaneously used to further validate the model's effectiveness.[13,72−74]

https://doi.org/10.1021/acsomega.6c00999
ACS Omega XXXX, XXX, XXX−XXX

Table 2. Empirical Formulas for Thermophysical Parameters[64−66]

parameter	gas phase	solid phase
heat capacity (J/kg.k)	$C_{p,g} = 945 + 0.3 \cdot T_g - 7.0 \times 10^{-5} \cdot T_g^2$	$C_{p,s} = 674 + 0.387 \cdot T_s - 1.08 \times 10^{-7} T_s^2$
heat conductivity (W/m.k)	$\lambda_g = 0.15\exp(-570/T_g)$	$\lambda_s = 0.08 \cdot T_s^{0.6}$
density (kg/m^3)	$\rho_g = P_g/RT_g \sum_i \frac{Y_i}{M_i}$	$\frac{1}{\rho_s} = \sum_j \frac{w_j}{\rho_j}$
viscosity (kg/m.s)	$\mu_g = 4.244 \times 10^{-5}(0.001T_g)^{0.652}$	-

This model is calculated by commercial CFD software. The temperature of the gas and solid is calculated using local nonthermodynamic equilibrium in the energy equation. The non-steady-state term, diffusion term, and source term are all defined through the user-defined function of Fluent software. To eliminate computational errors caused by the grid, grid independence verification was conducted. The k-ε turbulence model and a generalized finite rate model were adopted; the SIMPLE algorithm was used for the pressure velocity coupling; and the second-order upwind scheme was adopted for the discretization of turbulent kinetic energy and dissipation rate.

3.1. Sintering Cup Experiment for Coke Sintering Process

Yang's work[67,68] has received extensive attention and adoption in the industry due to its excellent data openness. Therefore, it was adopted to validate the proposed model for the sintering using only coke as fuel.

3.1.1. Main Boundary and Initial Conditions. Table 3 lists the main boundary and initial conditions, Table 4 presents the technical analysis and elemental analysis of coke and biochar.

Table 3. Partial Boundary Conditions and Initial Conditions

parameter	value
grid size/m	$\Delta x = 0.002, \Delta y = 0.002$
time step/s	1
initial mixture porosity	0.4
sintering bed height/m	0.60
iron ore diameter/mm	3.2
flux diameter/mm	1.6
coke diameter/mm	1.6
biochar diameter/mm	1.6
average diameter of bed particles/mm	3.2
proportion of iron ore/wt %	83.2
proportion of flux/wt %	13
proportion of coke/wt %	3.8
proportion of water/wt %	7
proportion of biochar/wt %	0
ignition time/s	90
ignition temperature/K	1373.15
ignition negative pressure/kPa	10
sintering negative pressure/kPa	15

3.1.2. Numerical Solution Method. A two-dimensional model of 0.02 × 0.60 m^2 was built in the center of the sintering cup. The region from the material surface to a depth of 0.57 m was the raw material, and the depth of the hearth layer was 0.03 m at the bottom. The simulation area was discretized by a structural grid. A schematic diagram of the sintering cup experiment and the computational domain is provided in Figure 4. The outlet temperature of 400 K and an initial temperature of the mixture of 300 K are set in the study. A minimum grid size of 0.002 m is used. Three thermocouples were installed in the upper (y = 0.11 m), middle (y = 0.3 m), and lower bed layers (y = 0.49 m) of the sintering cup to measure their corresponding temperature values. The waste components and flow rate are measured by the gas analyzer and flow meters installed at the wind box and outlet.

3.1.3. Comparison of Experimental Simulation Results. The comparison curves between the calculated and measured temperatures at the typical bed layers of the sintering machine are shown in Figure 5. PT is defined as the maximum temperature of solid materials at certain height locations of the sintering bed. As shown in Table 5 and Figure 5a, the PT is in good agreement with the measured data from the three thermocouple positions with relative errors of 9.98%, 8.84%, and 8.20%, respectively. The temperature curve shapes at different sintering positions are very similar to peak temperatures gradually increasing as the depth increases. This demonstrates the high heat-transfer and thermal-storage effects of the sintering bed. However, there are slight deviations between some simulated high-temperature zones and the measured values. The reason for this deviation may be that this paper simplifies the shrinkage and porosity models of the sintering bed. This model considers the impact of some factors in a linear manner, as shown in eq 35, which inevitably leads to some discrepancies with reality. These models cannot be directly measured during melting, and there have been no accurate empirical models available until now.

Figure 5b shows that during the ignition and insulation stages, gases CO_2 and CO are rapidly released to a peak (approximately 14.5% and 1.9%) due to fuel combustion, while the trend of O_2 is opposite (5.8%), as combustion consumes oxygen. After ignition, from about 200 to 1200 s, the O_2, CO_2, and CO contents in the sintering state stabilize (approximately 12.5%, 12.2%, and 1.5%, respectively) until the end of sintering, which is also called the steady-state sintering stage. A difference between the calculated and experimental flue gas compositions is observed near the end point of sintering, and the calculation process is slightly slower than that of the sintering pot experiment. This finding is probably because the coke size assumption in the coke combustion model is based on the average size of coke within each particle size range. The porosity of the bed layer will also vary accordingly, which differs from the facts.

Combustion and sintering characterization during the sintering process are applied to evaluate the process. Therefore, it is crucial to conduct a quantitative assessment of the thermal characteristics of simulation results. Previous researchers have gradually established a set of indicators linked to the sintering thermal state, as shown in Table 6, and this paper continues to adopt this evaluation system.

3.2. Sintering Cup Experiment for Biochar Sintering Process

Currently, in the literature on sintering numerical simulation, besides Wonyang,[67] the research group of Fan and Gan[13,72−74] has also provided good comparison sources for biochar sintering, and their data have maintained good integrity, consistency, and openness in previous published articles. The author has provided two substitution rates of 0% and 40% and compared the results of two biochar particles, 2.0 and 3.1. It can be clearly seen that the temperature calculation error and the trend of high-temperature zone holding time are similar, and the

https://doi.org/10.1021/acsomega.6c00999
ACS Omega XXXX, XXX, XXX−XXX

Table 4. Technical Analysis and Element Analysis of Coke and Biochar[a]

fuel	chemical composition (wt %-daf)					industrial analysis (wt %-db)			calorific value (MJ/kg)
	C	H	O	N	S	FC	VM	ASH	
coke	87.86	0.63	9.42	1.55	0.54	83.75	2.26	13.99	26.35
oak-charcoal[75]	78.11	2.54	18.75	0.48	0.12	55.60	27.10	17.30	23.05

[a]Db: dry basis; daf: dry ash-free basis; FC: fixed carbon; VM: volatile matter; ASH: wave points.

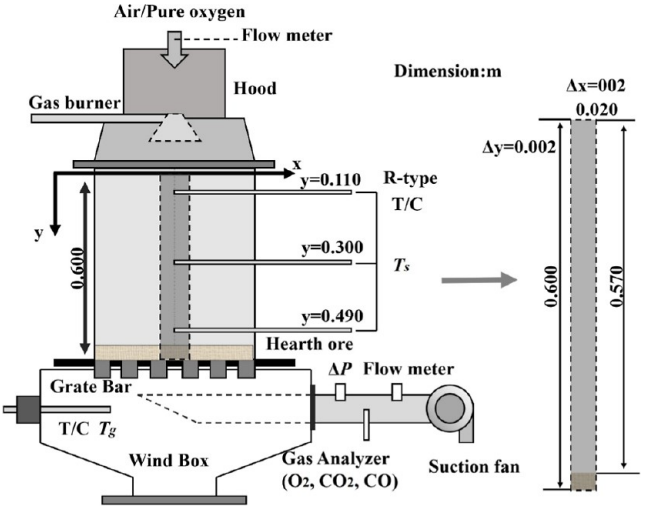

Figure 4. Sintering cup experiment and computation domain.

temperature curve shape is also very similar, as shown in Figure 6, Table 7, Table 8, and Table 9. Since previous studies on sintering with biochar replacing coke were mostly based on laboratory settings with relatively single processes, there are already relatively extensive experimental results and industry consensus. The detailed discussion and mechanism analysis on the results of the coarsening particle size in the following text not only serve as the basis for in-depth research but also can be regarded as a verification of the trend of detailed model results.

In addition, numerical simulation provides a relatively effective research method for low-carbon sintering that

Table 5. Comparison Between the Simulated and Measured PT

parameter	peak temperature, (K)		
	y = 0.11	y = 0.30	y = 0.49
calculated	1470.00	1502.00	1534.00
measured	1633.00	1666.00	1671.00
error (%)	9.98%	8.84%	8.20%

Table 6. Definition of Quantitative Parameters[68]

parameter	definition
flame front speed (FFS)	$\text{FFS} = \frac{\text{distance between two points}}{\text{time consumed propagation}}$ 17
heat front speed (HFS)	$v_h = \frac{c_{p,g} \cdot W}{c_{p,s}(1-\varepsilon)}$ [76]
sintering time (ST)	elapsed time until the flue gas temperature indicates maximum
peak temperature (PT)	peak value of bed temperature at a certain location
melting quantity index (MQI)	$\text{MQI} = \int_{t_1}^{t_2} (T_s - T_m) dt$. [15,77]
combustion zone thickness (CZT)	thickness of the zone whose solid temperature is over the initiation of char combustion (973.15 K)
melting zone thickness (MZT)	thickness of the zone whose solid temperature is over the iron ore melting (1373.15k)
duration time in the combustion zone (DTMZ)	time of temperature above 973.15 K
duration time in the melting zone (DTMZ)	time of temperature above 1373.15 K
yield	melt fraction range 0.2−0.4 [20][47]

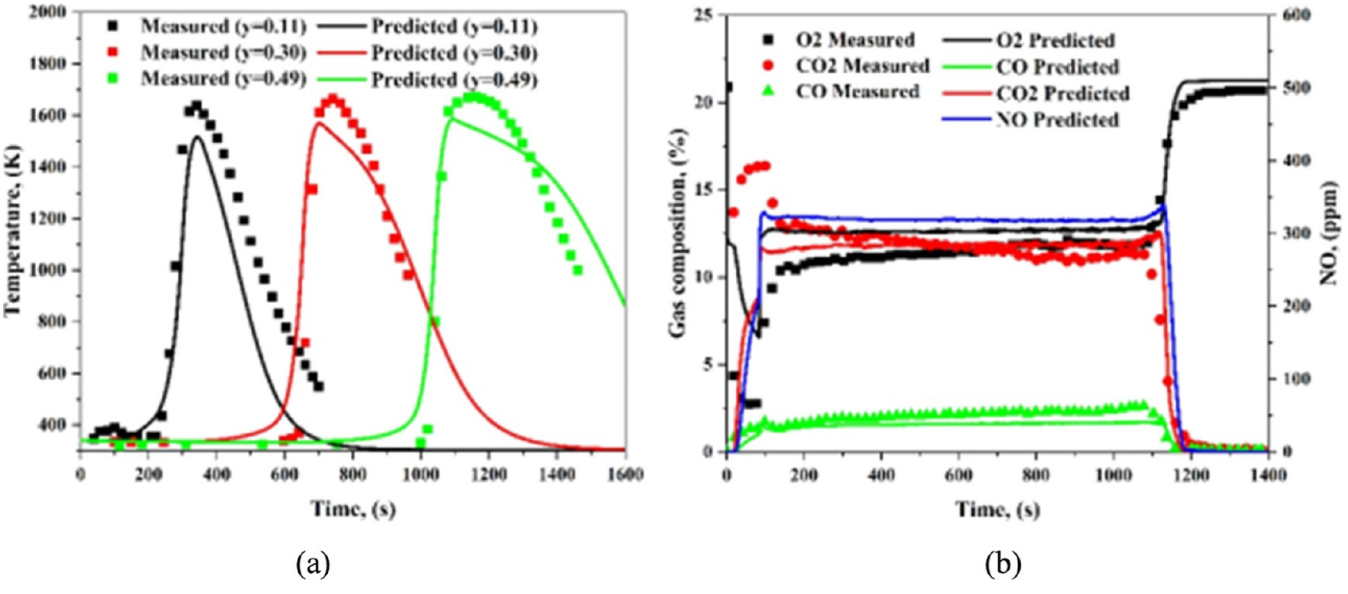

Figure 5. Comparison between the measured data and simulation results of (a) temperature profiles and (b) waste gas compositions.

https://doi.org/10.1021/acsomega.6c00999
ACS Omega XXXX, XXX, XXX−XXX

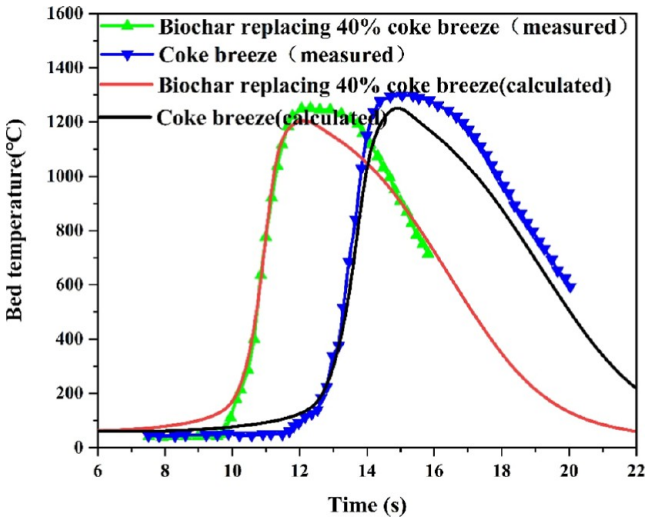

Figure 6. Comparison of temperature curves between measured and calculated values.

combines biochar substitution with multiple clean processes (such as hydrogen-rich injection, oxygen enrichment, flue gas circulation, fuel layering distribution, etc.), which can reduce the drawbacks of single-sintering cup experimental processes in the past. Currently, there is very little open experimental data on biochar sintering with multiple process combinations, and our research precisely has this advantage of handling the working conditions of multiple process combinations.

4. ANALYSIS OF SINTERING CHARACTERISTICS UNDER 60% BIOCHAR SUBSTITUTION

To make full use of the inherent properties of biochar to enhance the sintering process and quality, based on the typical high-proportion biochar-equivalent thermal replacement sintering, the combustion and sintering characteristics of coarsened biochar particle sizes (case 2−case 10:1.6−4.8 mm) were simulated and analyzed in detail. Furthermore, the NO emission characteristics of high-proportion large-diameter biochar sintering and the problem of unburned areas near the inlet of the sintering were analyzed. It is planned to adopt oxygen-enriched methods to improve fuel utilization efficiency. The unburned areas for the 3.2 mm and 4.8 mm biochar sintering cases (cases 6 and 10) were determined to be 318s and 818s after sintering, respectively. Then, selective oxygen-enriched injection was performed in these areas, forming cases 11−22. The simulation work was carried out according to the arrangement in Table 10.

4.1. Thermal Index Characteristics

Table 11 presents a comparison of the calculated thermal index results for different biochar diameters in the case studies. These values are the arithmetic means obtained at five bed depths (y = 0.1, 0.2, 0.3, 0.4, and 0.5 m).

In the case of isothermal replacement sintering with 1.6 mm biochar diameter and 60% proportion (case 2), due to the excellent combustion performance of biochar, the flame front speed (FFS) (2.63 cm/min) is higher than that of coke sintering (case 1:2.52 cm/min), and both the duration of the combustion zone (DTCZ) and the ST are reduced. The asynchrony between the FFS and the heat front speed (HFS) leads to a decrease in heat utilization, and other thermal indicators of sintering deteriorate significantly. Compared with coke sintering (case 1), the average PT of 60% biochar isothermal replacement sintering (case 2) is 1345.15 K, which is an 8.12% decrease. The melt quantity index (MQI), duration of the melting zone (DTMZ), cooling rate (CR), and yield are all 0. This indicates that the temperature of 60% biochar sintering does not reach the qualified melting rate of 20%, and the overall state is insufficient in heat, which is consistent with the conclusion mentioned above. High-proportion biomass fuel replacement faces the problem of deteriorating thermal indicators during the sintering process.

Figure 7 first presents the distributions of solid temperature and melt fraction for biochar with diameters of 2.8 mm and 4.8 mm. It is evident that as the biochar diameter increases, the thickness of the high-temperature zone, the overall temperature of the bed, and the melt fraction gradually increase. For the sintering with a 1.6 mm biochar diameter (case 2), the melt fraction is 0, and the initial melting temperature of 1373.15 K is not reached at any position in the bed. In the sintering with a 2.8 mm biochar diameter (case 5), there are signs of partial melting in the high-temperature region, but the melt fraction in the bed never reaches 0.2. However, in the sintering with 4.8 mm diameter biochar (case 10), the maximum melt fraction clearly exceeds 0.2 in some parts, meeting the definition standard for qualified products, and is mainly concentrated in the middle and lower parts of the bed. In the sintering with large-diameter biochar (case 10), there is still obvious heat accumulation and uneven heat distribution. The overall insufficient heat in the near-inlet region of the sintering tends to intensify, which may further limit the yield of the sintered ore products.

Figure 8 details the trend of the average values of the thermal indicators under coarsened biochar particle sizes. As shown in Figure 8a, with the increase in biochar diameter, the FFS gradually decreases, and the ST increases. This indicates that using the method of coarsening the particle size can inhibit the high reactivity of biochar fuel, reducing its combustion speed. The matching gap between the HFS and the FFS shows a trend

Table 7. Comparison of Maximum Temperatures[a]

item	replacement %	layer1 T_{max}/°C	layer2 T_{max} /°C	layer3 T_{max} /°C	layer4 T_{max} /°C
measured	0	1250	1305	1328	1351
calculated	0	1118	1251	1273	1285
error	10.56%	4.13%	4.14%	4.88%	
measured	40	1212	1255	1290	1315
calculated	40	1105	1205	1224	1232
error	8.83%	3.98%	5.12%	6.31%	

[a]Layers 1 to 4 are depths of 85 mm, 255 mm, 425 mm, and 595 mm, respectively.

https://doi.org/10.1021/acsomega.6c00999
ACS Omega XXXX, XXX, XXX−XXX

Table 8. Comparison of High-Temperature Holding Time[a,b]

item	replacement %	layer1 $t \geq 1200$ °C,s	layer2 $t \geq 1200$ °C,s	layer3 $t \geq 1200$ °C,s	layer4 $t \geq 1200$ °C,s
measured	0	72	162	282	258
calculated	0	9	148	264	395
measured	40	42	108	192	210
calculated	40	12	136	249	376

[a]Considering that the temperature results we calculated are relatively low, we used $t \geq 1100$ °C for display. [b]Layers 1 to 4 are depths of 85 mm, 255 mm, 425 mm, and 595 mm, respectively.

Table 9. Comparison under Different Diameters of Biochar[a]

item	mean diameter of biochar	layer2 (255 mm)	$t \geq 1200$ °C,s
measured	2.4	1255	108
calculated	2.4	1205	134
measured	3.1	1281	120
calculated	3.1	1221	134

[a]Considering that the temperature results we calculated are relatively low, we used $t \geq 1100$ °C for display.

Table 10. Computational Cases Arrangement

no	substitution rate	biochar diameter	oxygen enrichment parameters		
			time	conc	segregation
case 1	0%	-	-	-	-
case 2	60%	1.6 mm	-	-	-
case 3	60%	2.0 mm	-	-	-
case 4	60%	2.4 mm	-	-	-
case 5	60%	2.8 mm	-	-	-
case 6	60%	3.2 mm	-	-	-
case 7	60%	3.6 mm	-	-	-
case 8	60%	4.0 mm	-	-	-
case 9	60%	4.4 mm	-	-	-
case 10	60%	4.8 mm	-	-	-
case 11	60%	3.2 mm	318	0.25	-
case 12	60%	3.2 mm	318	0.29	-
case 13	60%	3.2 mm	318	0.33	-
case 14	60%	4.8 mm	818	0.25	-
case 15	60%	4.8 mm	818	0.29	-
case 16	60%	4.8 mm	818	0.33	-
case 17	60%	3.2 mm	318	0.25	0.29−0.21
case 18	60%	3.2 mm	318	0.29	0.37−0.21
case 19	60%	3.2 mm	318	0.33	0.45−0.21
case 20	60%	4.8 mm	818	0.25	0.29−0.21
case 21	60%	4.8 mm	818	0.29	0.37−0.21
case 22	60%	4.8 mm	818	0.33	0.45−0.21

of first decreasing and then increasing. When the biochar diameter is between 2.0 mm and 2.4 mm, the matching gap is between 1.78% and −0.88%, which means that FFS and HFS match well and the thermal utilization performance is perfect. Therefore, the optimal "matching" diameter of biochar and v-coke must also be within this range. As the diameter of biochar becomes larger and larger, the matching between FFS and HFS is gradually disrupted. At a large biochar diameter of 4.8 mm, the difference reaches 10.99%, which will increase the asynchronous trend of the combustion of the two solid fuels, thereby weakening the combustion focus of solid fuels and further leading to new changes in thermal indicators, such as PT, DTMZ, and MQI.

Figure 8b,c shows the average PT, DTCZ, yield, DTMZ, MQI, and CR values under coarsened biochar particle sizes. The average PT, CR, DTMZ, and yield all show a trend of first increasing and then decreasing with the increase in biochar particle size, while the average combustion zone residence time DTCZ and melt quantity index MQI show a continuous increasing trend, but the growth trend gradually slows down under large diameters. This indicates that there is an upper limit to the improvement effect of coarsening particle size on thermal indicators. The biochar diameters corresponding to the extreme value inflection points of each indicator are not the same, generally in the diameter range of 2.4−4.0 mm. For example, from the perspective of yield, when the biochar diameter is less than 2.8 mm, the bed temperature can never reach the 20% melting rate level. However, when the biochar diameter increases to 3.2 mm, the yield increases from 0 to 39.27%. When the biochar diameter is 4.0 mm, the yield reaches its upper limit of 46.88%. When the biochar diameter continues to increase, the yield gradually decreases and remains at the 40% level. Compared with the yield of 77.84% in standard coke sintering (Table 8: case 1), there is still a large gap. The situation of other indicators is similar. It is obvious that the process should be continuously improved to make its sintering level reach or approach the level of the full-coke method.

Figure 9 shows a comparison of temperature curves at various bed depths during sintering under different biochar diameters. It can be seen from Figure 9a,b that, compared with the sintering of biochar with a diameter of 1.6 mm (case 2), the temperatures in the bed layer ($y > 0.3$ m) during the sintering of biochar with diameters of both 2.8 mm and 4.8 mm show an increasing trend. However, in the near-inlet region of the sintering bed ($y < 0.2$ m), especially when $y = 0.1$ m, the temperature curve of the sintering of biochar with a diameter of 2.8 mm shows an increase, while that of biochar with a diameter of 4.8 mm shows a

Table 11. Average Values of Thermal Indicators for Different Cases (Diameter Groups)

no	FFS (cm/min)	PT (K)	DTCZ (s)	DTMZ (s)	MQI (K·s)	CR (K/min)	ST (s)	yield (%)
case 1	2.52	1464.01	55.2	165.6	9671.34	65.40	1358	77.84
case 2	2.63	1345.15	52	0	0	0	1300	0
case 5	2.43	1403.27	61.6	93.2	3040.08	35.65	1406	0
case 10	2.24	1374.93	94.4	98.8	5797.03	32.64	1530	44.22

https://doi.org/10.1021/acsomega.6c00999
ACS Omega XXXX, XXX, XXX−XXX

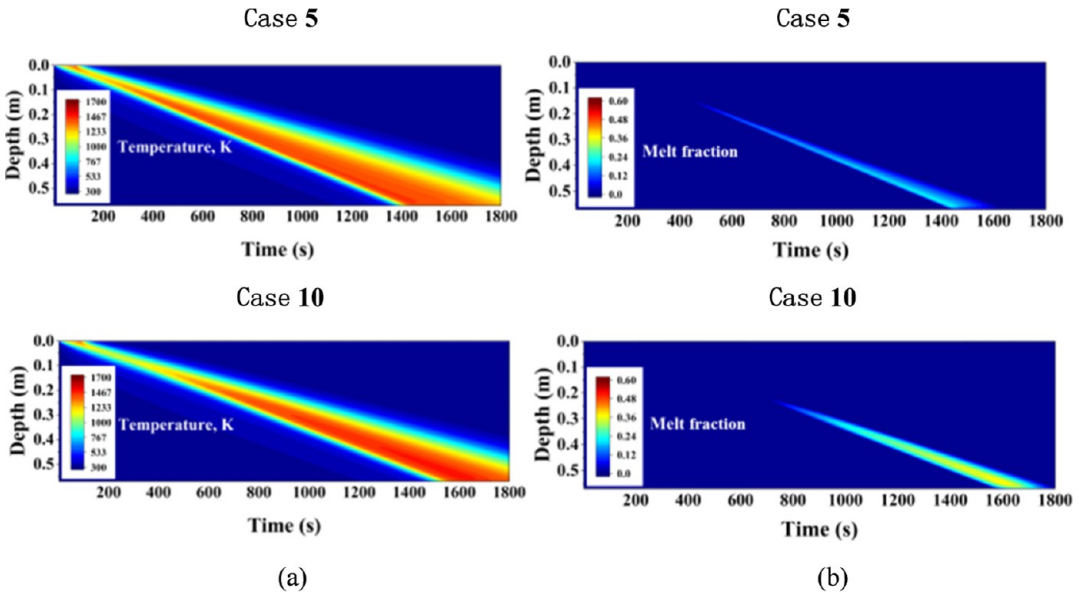

Figure 7. distributions with cases 5 and 10: (a) solid temperature; (b) melt fraction.

decreasing trend. The temperature curve results at the bed depth of y = 0.1 m for each biochar diameter are specifically extracted, as shown in Figure 9c. It can be roughly seen from the figure that when the biochar diameter is less than 3.2 mm, the temperature at the bed depth of y = 0.1 m is generally enhanced; when the biochar diameter is greater than 3.2 mm, the opposite effect occurs, and the temperature curve in the near-inlet region shows a downward trend. This indicates that although various average indicators of the sintering of large-diameter biochar are improved and the yield of qualified products is significantly increased, the temperature deterioration trend in the near-inlet region is also significant, which has become a bottleneck restricting the further improvement of the sintering quality in large-diameter biochar. In addition, the thermal curves after coarsening the particle size also show a simultaneous increase in the ST, which means that the sintering speed is effectively inhibited.

To further study the combustion characteristics of biochar sintering with different diameters, Figure 10 extracts the temperature contour maps of cases 2, 5, and 10 at 300 and 1200 s. These two time periods can represent two bed depth positions: the near-inlet region of the sintering and the lower bed layer of sintering. It can be seen from Figure 10a,b that as the diameter of biochar increases, the thickness of the high-temperature zone (including the entire combustion zone and melting zone) becomes thinner. The combustion zone thickness (CZT) and the melting zone thickness (MZT) are defined as the thicknesses of the regions where the temperature is set above 973.15 and 1373.15 K, respectively. Therefore, they are highly dependent on the temperature of the sintering bed. Since there is iron ore liquid melt in the high-temperature region, CZT and MZT will significantly affect the permeability of the sintering bed. Considering the heat accumulation effect along the depth of the sintering bed, in the same sintering case, CZT and MZT will inevitably increase gradually with depth, as shown in Figure 11. Taking 2.8 mm biochar sintering as an example (case 5), at 300, 750, and 1200 s, the CZT values are 24 mm, 72 mm, and 115 mm, respectively, while the MZT values are 0 mm, 29 mm, and 60 mm, respectively, all increasing with the enhancement of the heat accumulation effect in the bed depth. When comparing different biochar sintering cases, the larger the diameter, the thinner the CZT and MZT, which is consistent with the intuitive visual impression in the temperature contour maps. For example, in the case of 4.8 mm biochar sintering, the CZT values are 15 mm (−37.5%), 48 mm (−33.33%), and 76 mm (−33.91%), respectively, while the MZT values are 0 (0%), 16 (−44.83%), and 58 (−3.33%), respectively. Compared with 2.8 mm biochar sintering, both thickness indicators showed reductions to varying degrees. The thinning of the combustion zone and melting zone may have an adverse effect on the quality of sintered ore because the thinning of the zone thickness may mean a simultaneous reduction in the high-temperature holding time. For example, the DTMZ in Figure 11c also shows a trend of time shortening under large diameters, while the DTCZ in Figure 11b shows a slowing of the rising trend. Considering that the CZT becomes thinner and thinner under large diameters, the time inflection point should appear at a larger diameter (>4.8 mm).

The local thermal indices for different biochar diameters and different bed depths are listed in Figure 12. It can be found that at specific positions in the lower bed layer, such as bed depths of y = 0.4 m and y = 0.5 m, all five local indices increase with the increase in biochar diameter. However, in the upper bed layer (y < 0.2 m), such as bed depths y = 0.1 m and y = 0.2 m, the local indices all show a trend of first rising and then falling as the diameter increases. This indicates the local differentiation effect of the coarsened biochar particle size along the depth of the sintering bed. The near-inlet area shows a trend of deterioration in local indices, and the deterioration trend becomes more intense and spreads as the diameter increases. This will limit the growth of average indices, showing the limitations of using the method of coarsening the particle size to enhance biochar sintering.

4.2. Waste Gas Emissions and Reaction Rate

The main exhaust gas concentration curves of biochar sintering with diameters of 1.6 mm and 4.8 mm (case 2 and case 10) were extracted, as shown in Figure 13. Figure 14 also details the NO emission concentration curves and the comparison of average emission concentrations (average from 90 to 1200 s) for each biochar diameter. From the comparison between Figure 13a and

https://doi.org/10.1021/acsomega.6c00999
ACS Omega XXXX, XXX, XXX−XXX

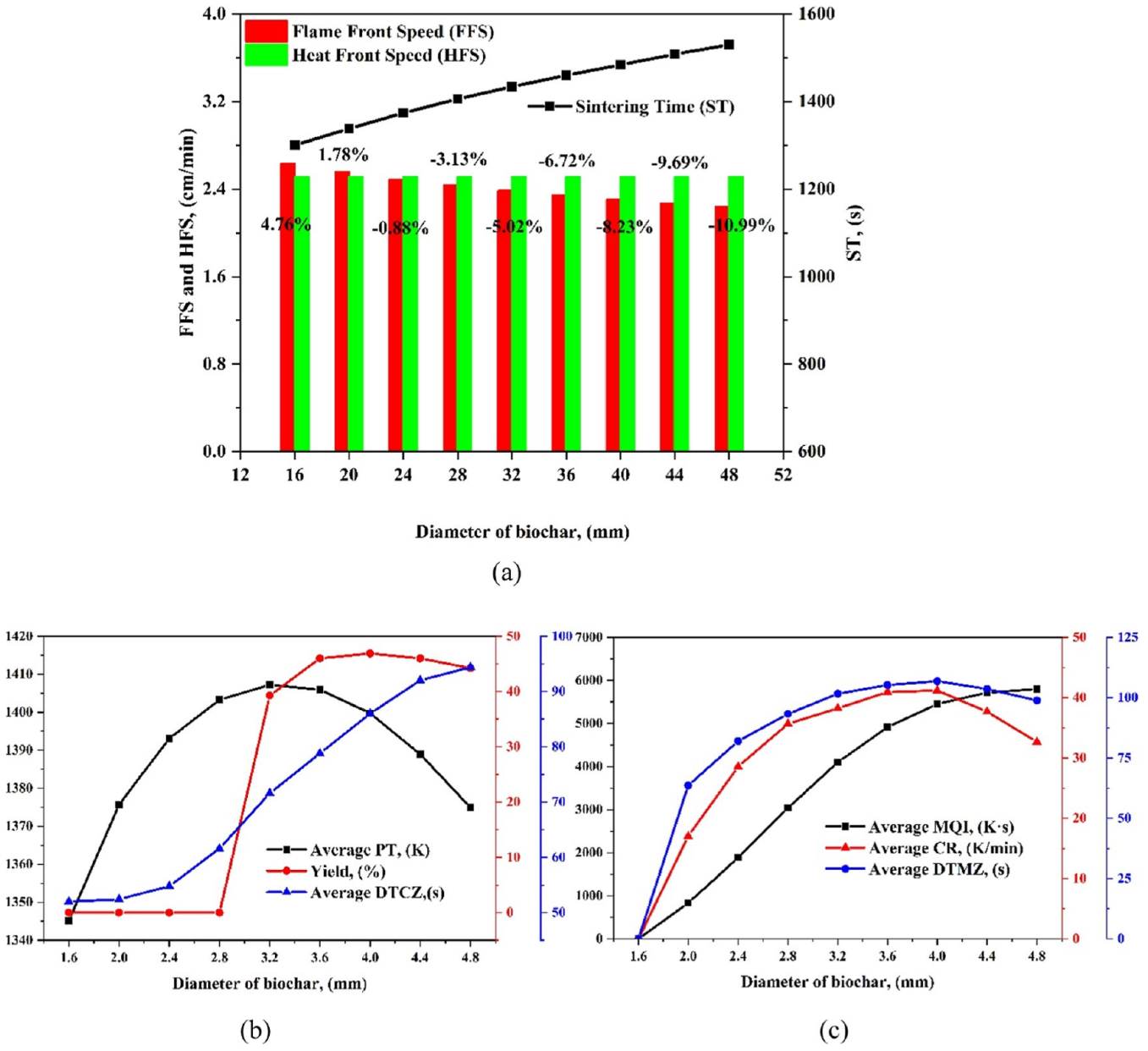

Figure 8. Thermal indicators between cases 2 and 10: (a) FFS and ST; (b) average PT, DTCZ, and yield; (c) average MQI, CR, and DTMZ.

b, it can be seen that with the increase in biochar diameter, the consumption of O_2 and the production of CO and CO_2 emissions in the exhaust gas decrease, while the concentration of H_2O shows almost no change. This indicates that the change in biochar diameter directly and mainly affects the chemical reaction formula.

Next are some secondary reactions involving CO, CO_2, O_2, etc. According to the formula for the rate of carbon oxidation reaction (see eq 20 in Table 1), when the diameter of fuel particles increases, the particle surface area will increase, but at the same time, the number of fuel particles per unit volume will decrease, and both the thickness and resistance of the gas passing through the particle layer will increase. This further reduces the chance of contact between oxygen and carbon. Overall, coarsening the particle size partially inhibits the high reactivity of biochar fuel, which is consistent with the previous trends of a decrease in FFS and an increase in ST. In addition, in Figure 13b, the curves of O_2, CO, and CO_2 in case 10 show a different arc-shaped trend from those in case 2 at approximately 90−400s. Looking back at the thermal curves in Figure 9b,c, there is an obvious correspondence between the two. The significant decrease in temperature in the near-inlet area during sintering leads to the arc-shaped trend of concentrations in the near-inlet area, which is closely related to the reduction in the reaction rate of char-N (see eq 30 in Table 1). Meanwhile, since Evans' empirical CO/CO_2 product ratio is used in this model (see eq 20 in Table 1), the dynamic stoichiometric number calculated at low temperatures will also decrease, which will result in a greater degree of incomplete combustion at low temperatures and a corresponding reduction in the total amount of CO and CO_2 generated.

Figure 14 further presents the results of NO and average CO_x emissions under different biochar diameters. It can be seen from Figure 14a that the NO emission decreases when the biochar particle size is coarsened. Since the release of char-N is the main part of NO generation (eq 30), and its reaction rate has a linear

https://doi.org/10.1021/acsomega.6c00999
ACS Omega XXXX, XXX, XXX−XXX

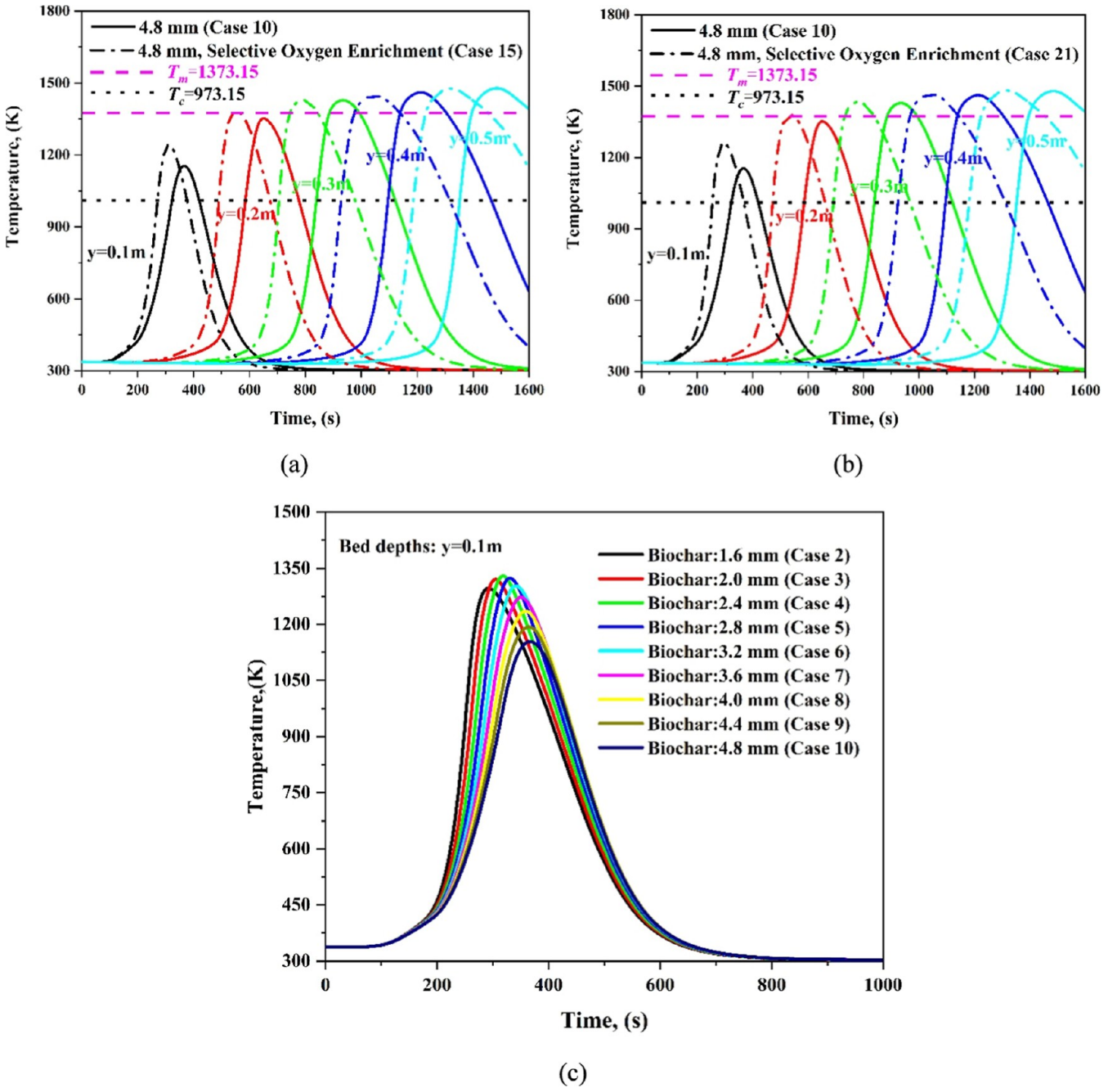

Figure 9. Temperature curves at different biochar diameters: (a) cases 2 and 5; (b) cases 2 and 10; (c) y = 0.1 bed depths.

positive correlation with the char reaction rate, the NO curve under the sintering of large-diameter biochar also shows an arc-shaped trend at approximately 90−400 s. Figure 14b shows that the generated CO and CO_2 are gradually decreasing, which is actually caused by the reduction in the reaction rate of R.11 char combustion. In general, coarsening the particle size is beneficial for reducing NO and CO_x emissions.

Figure 15 shows a comparison of the char combustion rates (eq 20) under sintering with different biochar diameters. Two typical times, 300 s and 1200 s, are selected to represent the near-inlet region of the upper sintering bed and the lower sintering bed, respectively. It can be seen from the figure that as the biochar diameter increases, the high reactivity of biochar is effectively inhibited and the char reaction rate also gradually decreases. For example, in Figure 15a,b, at the near-inlet region of the sintering bed, the maximum reaction rates of biochar for case 2 (1.6 mm diameter), case 5 (2.8 mm diameter), and case 10 (4.8 mm diameter) are 96.98 mol/m^3 s, 53.39 mol/m^3 s, and 24.77 mol/m^3 s, respectively. A similar downward trend is observed for biochar in the lower bed. At the near-inlet region of the sintering bed, the maximum reaction rates of char for case 2, case 5, and case 10 are 66.65 mol/m^3 s, 56.65 mol/m^3 s, and 42.36 mol/m^3 s, respectively, and they also show a downward trend in the lower bed, being 65.19 mol/m^3 s, 61.06 mol/m^3 s, and 52.65 mol/m^3 s. Obviously, after coarsening the particle size, the reduction in the reaction rate of coke and biochar helps to inhibit the high reaction rate of biomass fuels, thereby reducing the FFS and heat release rate. However, at the same time, it causes a further decrease in the temperature of the sintering near-inlet area, which already lacks a heat input.

https://doi.org/10.1021/acsomega.6c00999
ACS Omega XXXX, XXX, XXX−XXX

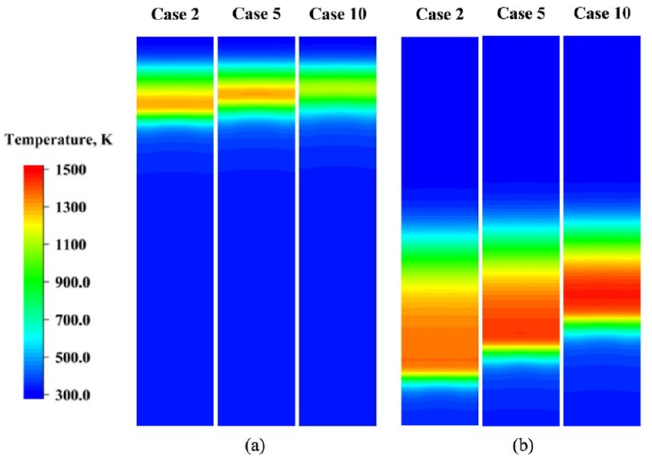

Figure 10. Temperature contours of cases 2 and 5 at (a) 300 s and (b) 1200 s.

4.3. Main Problems

Using the method of coarsening particle size can enhance various thermal indicators of coke/biochar and effectively suppress the high reactivity of part of biochar. However, the sintering of biochar under high proportions and large-diameter thermal substitution still cannot reach the normal sintering index level. Referring to Figure 8b, in the range of 3.6−4.8 mm biochar diameter, the yield generally exceeds 40%, but there is a large gap from the benchmark coke sintering yield of 77.84%. Further increase in the biochar diameter will be affected by the expansion of the temperature reduction range in the near-inlet area of the sintering bed, the decrease in the solid combustion rate, and the reduction in heat release, resulting in a gradual decrease in yield. Figure 16 specifically extracts the cloud maps of the remaining radius of sintered biochar with diameters of 1.6 mm, 2.8 mm, and 4.8 mm. In the case of a 1.6 mm biochar diameter, all solid fuels are completely burned during the sintering process. For the 2.8 mm diameter, the surface layer is unburned. For the 4.8 mm diameter, the unburned area accounts for about one-third of the bed. This shows that the problem of insufficient fuel utilization caused by coarsening particle size is very prominent, which is obviously an important reason for the temperature drop in the near-inlet area and insufficient yield in the sintering of large-diameter and high-proportion biochar. The solid fuel is not effectively utilized, and continuing to increase the particle size will be counterproductive. On the whole, the method of coarsening particle size still needs further improvement and optimization to further expand the availability of high-proportion and large-diameter biochar sintering.

5. IMPROVEMENT EFFECT OF SELECTIVE OXYGEN ENRICHMENT COUPLED WITH SEGREGATION

On the basis of the analysis in the previous text, simply using coarsened particle sizes will cause prominent problems, such as insufficient melting in the region near the sintering inlet and unburned fuel. According to the literature research, oxygen enrichment has a good effect on accelerating the reaction rate of solid fuels such as coke in sintering and improving incomplete combustion. This section mainly discusses the case results of improving biochar sintering by continuing to adopt the selective oxygen enrichment method on the basis of coarse particle sizes.

Cases 11−16 and cases 17−22 are relevant simulation cases using selective oxygen enrichment and selective oxygen enrichment coupled with segregation processes, respectively, for the sintering of high-proportion, large-diameter biochar. The precise locking of the region for selective oxygen enrichment injection depends on the remaining radius of biochar under the same biochar diameter, which is determined as the near-inlet region of the sinter where the biochar is not completely burned.

Figure 17 shows the comparison of average index conditions for biochar with a diameter of 4.8 mm (non-oxygen-enriched case: 10), as well as the selective oxygen-enriched injection cases (case 14:25%, case 15:29%, and case 16:33% oxygen concentration) based on it, and the selective oxygen-enriched coupled segregation cases (case 20:25%, case 21:29%, and case 22:33% oxygen concentration). Compared with case 10, both the selective oxygen-enriched injection and the selective oxygen-enriched coupled segregation injection have a significant increase in FFS, and the ST decreases accordingly. For example,

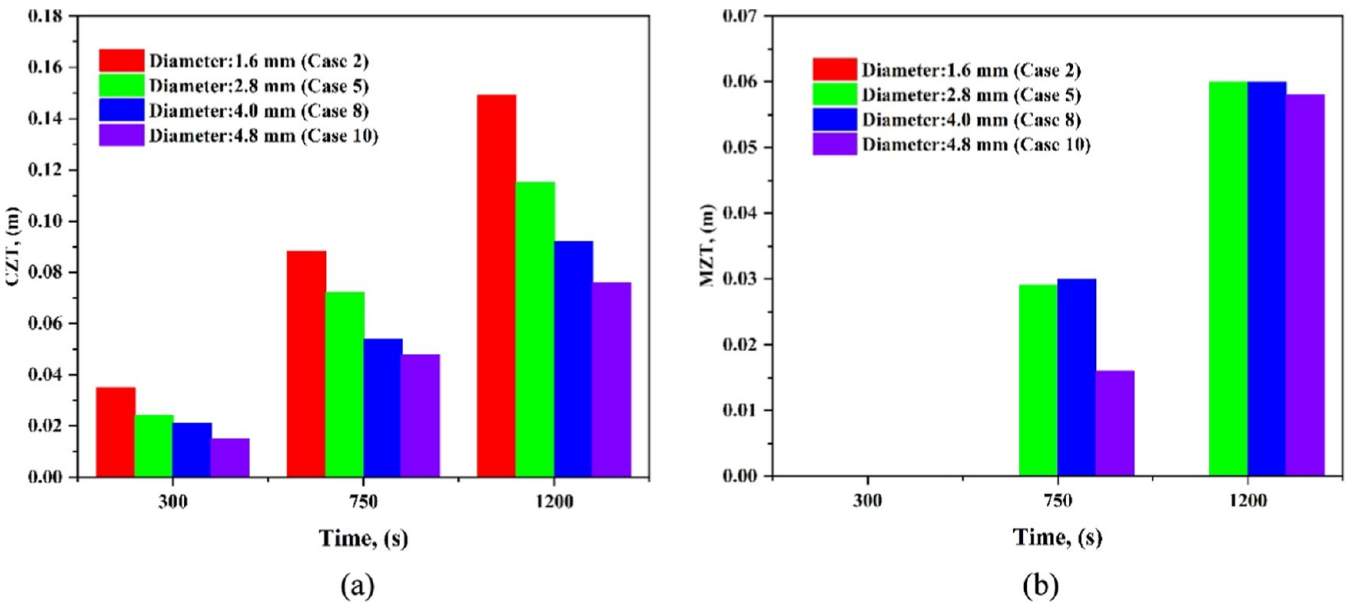

Figure 11. CZT and MZT of cases 2, 5, and 10 at 300 and 1200 s: (a) CZT and (b) MZT.

https://doi.org/10.1021/acsomega.6c00999
ACS Omega XXXX, XXX, XXX−XXX

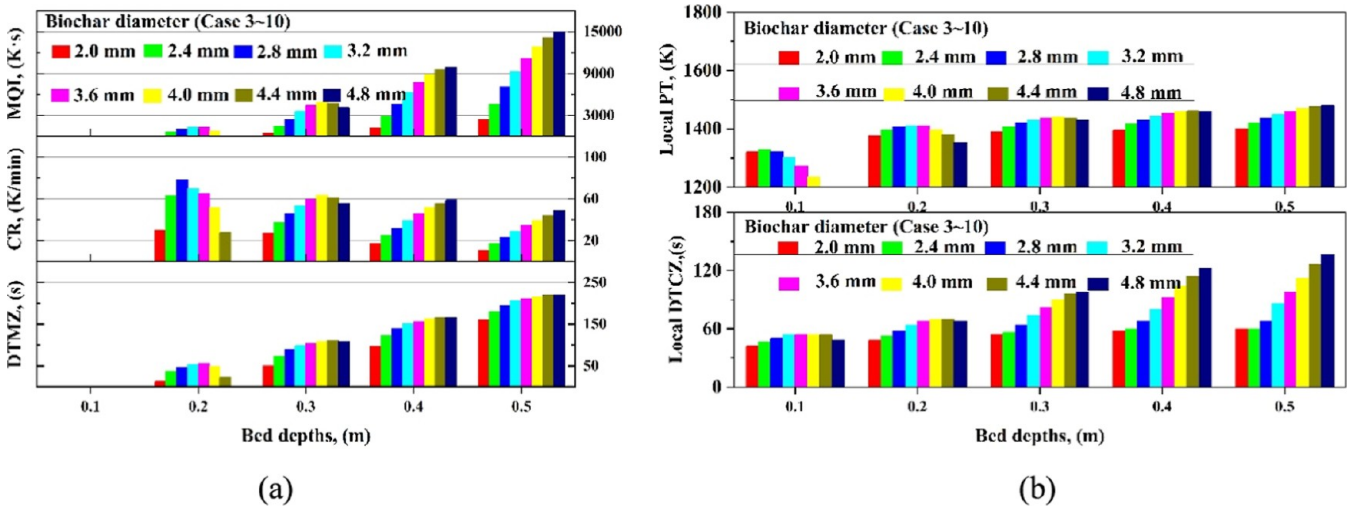

Figure 12. Comparison of indicators under different biochar diameters: (a) local MQI, CR, DTMZ; (b) local PT and DTCZ.

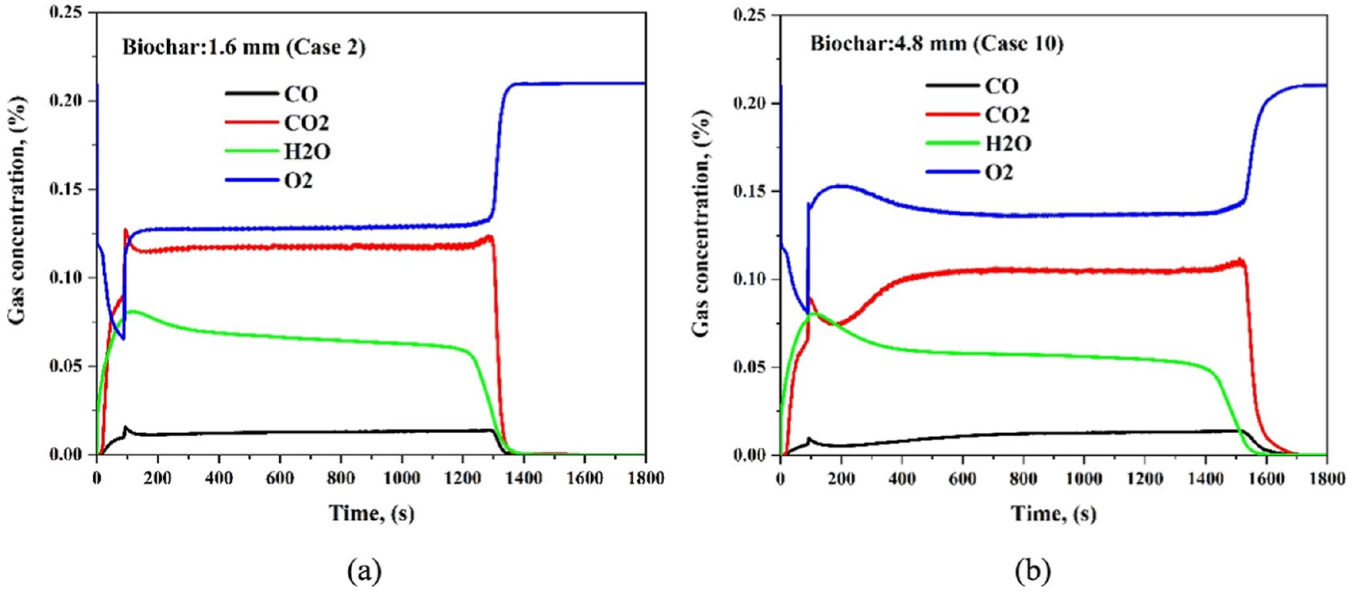

Figure 13. Comparison of waste gas composition: (a) case 2; (b) case 10.

in case 10, the FFS and ST are 2.24 cm/min and 1530 s, respectively, while in the selective oxygen-enriched case (case 15) and the selective oxygen-enriched coupled segregation case (case 21), the FFS values are 2.51 cm/min (+12.05%) and 2.51 cm/min (+12.05%), respectively, and the ST values are 1364 s (−10.85%) and 1360 s (−11.11%), respectively. Moreover, the ST and FFS index values of selective oxygen enrichment and selective segregation oxygen enrichment are at the same levels. From the comparison of the 33% oxygen-enriched cases (cases 16 and 22), the FFS and ST indexes of the selective oxygen-enriched coupled segregation process accelerate faster. The FFS and ST indexes reflect that oxygen enrichment accelerates the sintering speed.

In terms of the yield, oxygen enrichment slightly increased the yield. The yield in the non-oxygen-enriched case 10 was 44.22%, while that in both the selective oxygen-enriched cases 15 and 21 was 44.27% (+0.1%), showing almost no change. This indicates that the range of increase in the melting rate caused by the oxygen enrichment is limited. Considering that selective oxygen enrichment mainly acts on the area near the sintering inlet, the melting rate at this location may be limited. In terms of DTCZ and the duration of the melting zone (DTMZ), the DTCZ values in selective oxygen-enriched cases 15 and 21 were 91.2 and 92.8 s, respectively, which were slightly lower than the 94.4 s in the non-oxygen-enriched case 10. DTMZ showed the same trend. According to their respective definitions, this indicates that oxygen enrichment may narrow the average widths of the thermal curves in the combustion zone and the melting zone.

From the perspective of the melt quantity index (MQI) and the average PT, selective oxygen enrichment coupled with segregation slightly increases the average MQI, which is better than the case of oxygen enrichment without segregation. For example, the MQI of case 10 without oxygen enrichment is 5797.03 K·s, while in selective oxygen enrichment, case 15 shows 5477.57 (−5.51%), and case 21 shows 6316.07 (+8.95%). The selective oxygen enrichment coupled with the segregation process has a higher melt quantity index, which means higher sintering strength. Both selective oxygen enrichment methods increase the average PT. The PT of case 10 without oxygen enrichment is 1374.93K, and the peak temperatures of case 15

https://doi.org/10.1021/acsomega.6c00999
ACS Omega XXXX, XXX, XXX−XXX

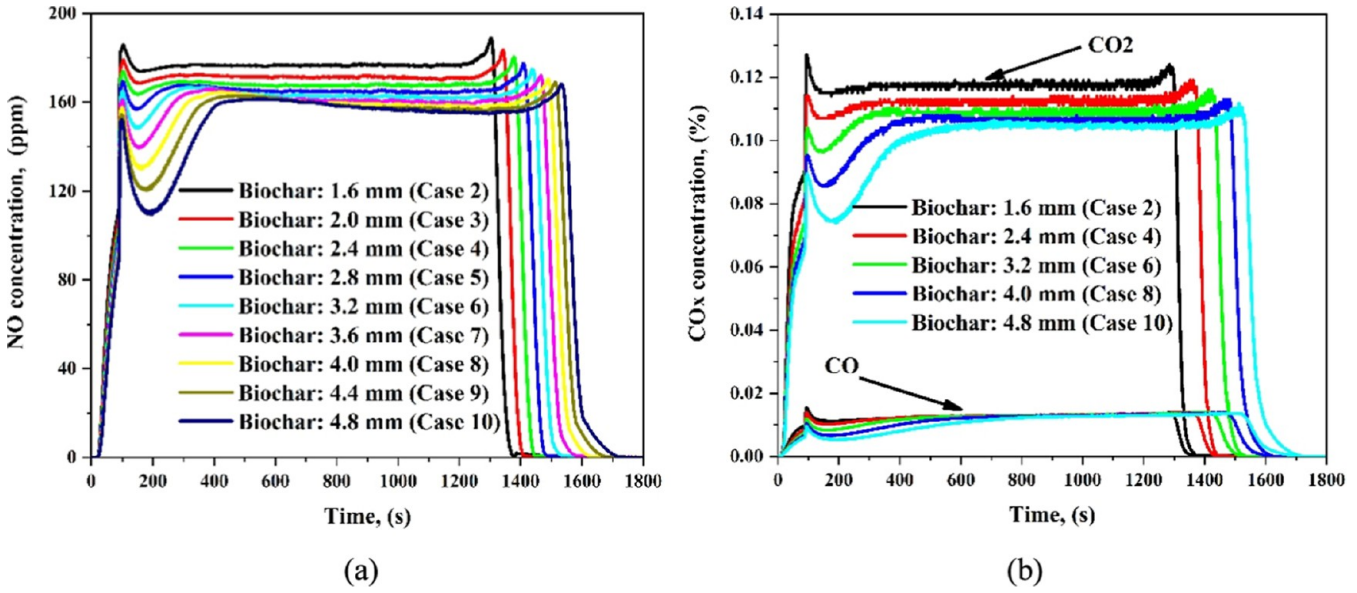

Figure 14. Comparison of pollutant emissions; (a) NO; (b) CO_x.

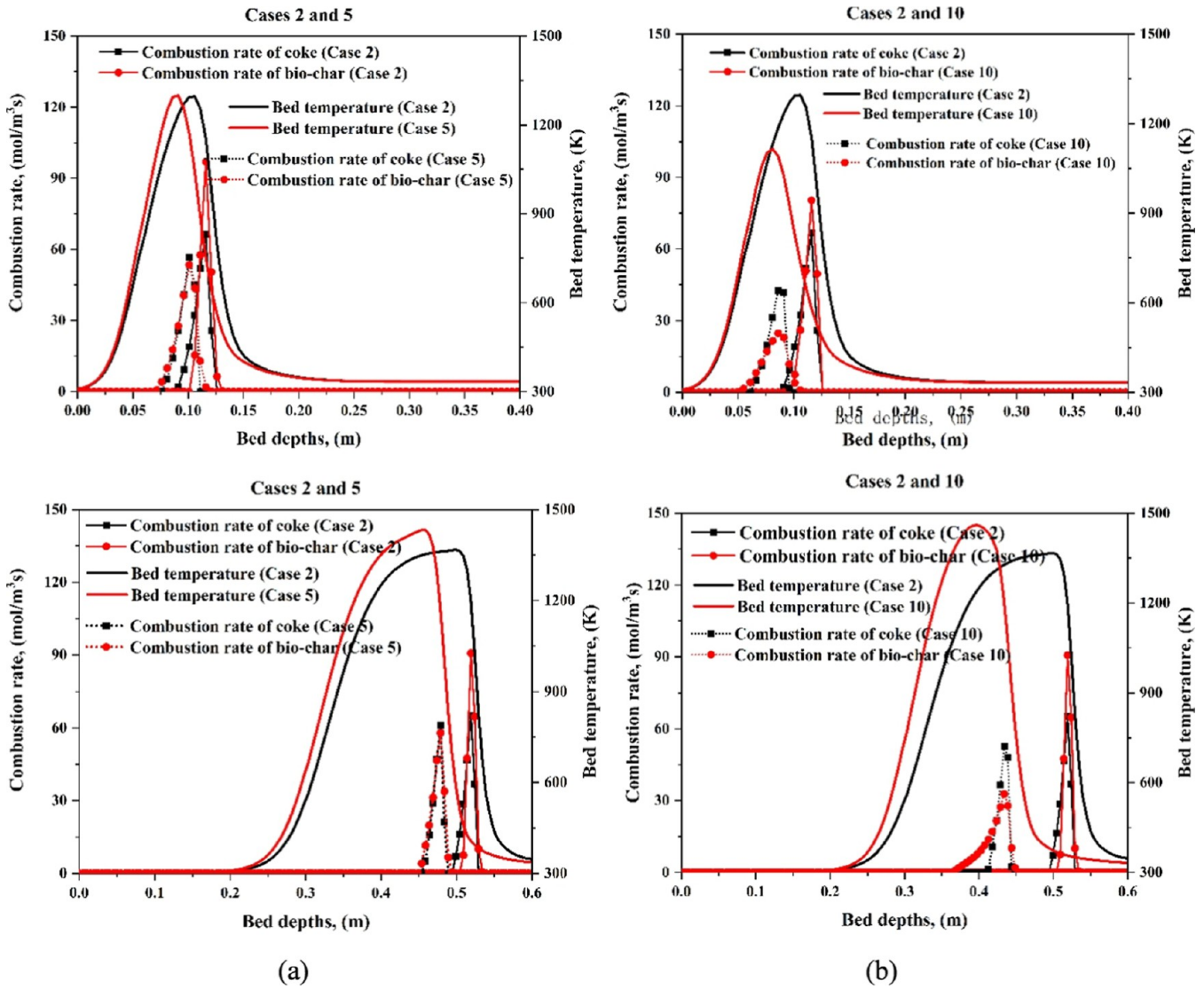

Figure 15. Combustion rates of coke-char and biochar with cases 2, 5, and 10: (a) 300 s; (b) 1200 s.

https://doi.org/10.1021/acsomega.6c00999
ACS Omega XXXX, XXX, XXX−XXX

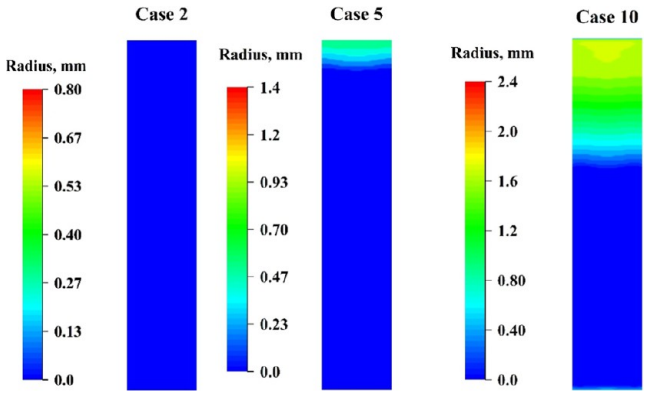

Figure 16. Residual radius of biochar under different diameter cases.

and case 21 are 1395.96K (+1.53%) and 1404.31K (+2.14%), respectively. Therefore, in terms of average indicators, the selective oxygen enrichment coupled with the segregation process is better than the case without segregation.

Figure 18 shows the temperature contour maps of cases 10, 15, and 21 with a diameter of 4.8 mm at 300 and 1200 s. It can be

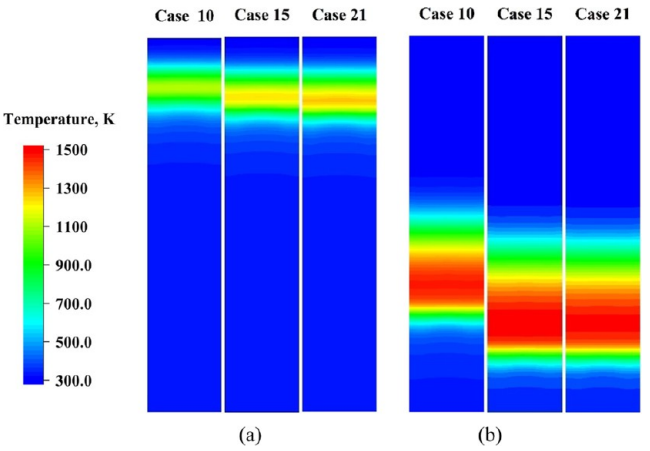

Figure 18. Temperature contours of cases 10, 15, and 21 at (a) 300 s and (b) 1200 s.

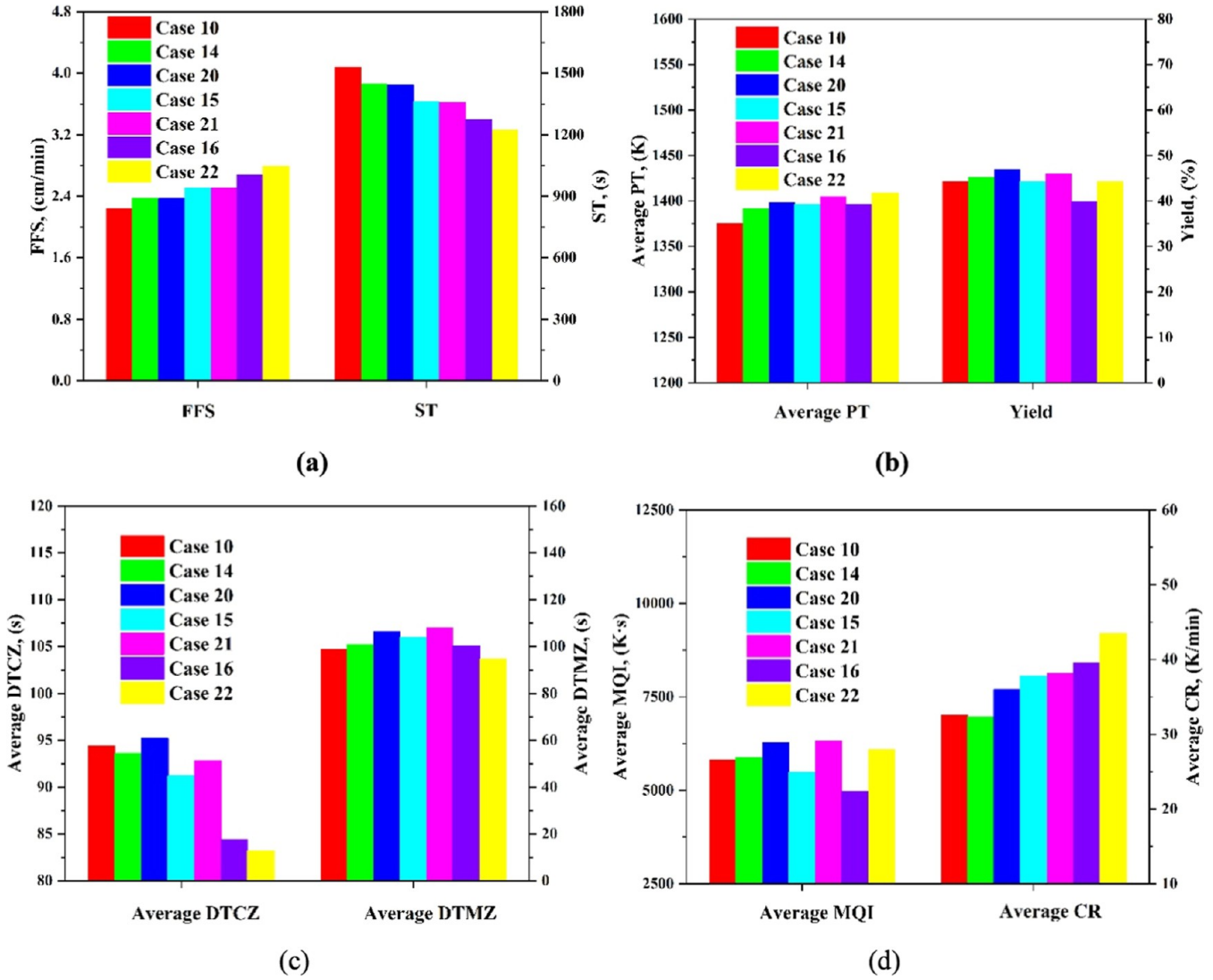

Figure 17. Comparisons of indicators with cases 10, 14, 20, 15, 21, and 26: (a) FFS and ST (b); average PT and yield; (c) average DTCZ and DTMZ; (d) average MQI and average CR.

https://doi.org/10.1021/acsomega.6c00999
ACS Omega XXXX, XXX, XXX−XXX

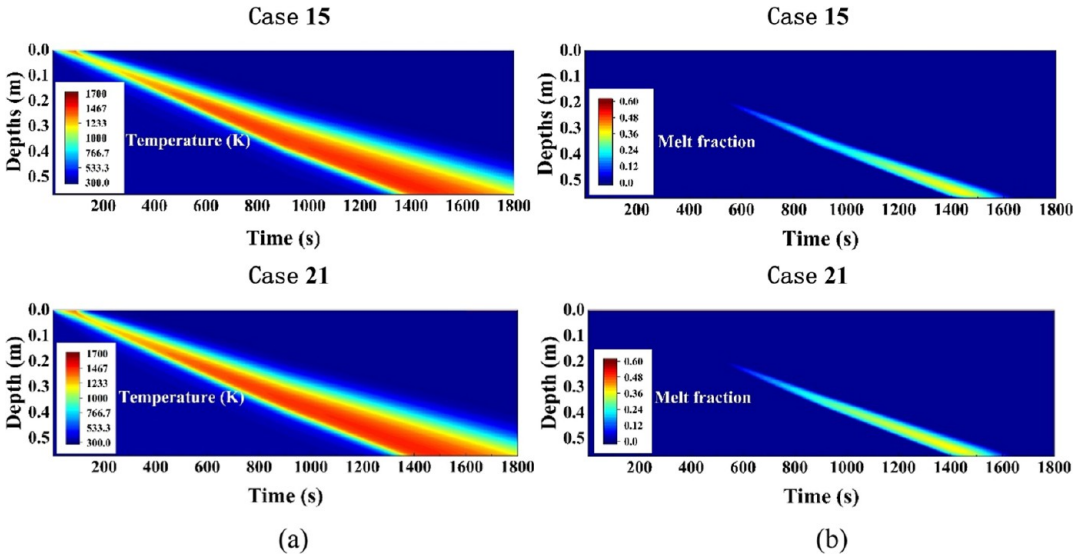

Figure 19. distributions with cases 15 and 21: (a) solid temperature; (b) melt fraction.

intuitively seen from Figure 18 that selective oxygen enrichment expands the high-temperature area in the upper bed, accelerates its downward movement, and increases the PT to some extent. Case 21, which involves selective oxygen enrichment coupled with segregation, is the most obvious. Figure 18b shows that in the lower bed, selective oxygen enrichment leads to a more significant expansion of the high-temperature red hot area. Meanwhile, the sintering rates of the two oxygen enrichment methods tend to be the same, moving downward side by side. This indicates that the temperature enhancement in the sintering inlet area is transmitted to the lower layer due to the heat storage effect. Figure 19 presents the two-dimensional temperature and melt distribution of cases 15 and 21 along the length of the sintering machine. By comparison with case 10 in Figure 6, it can be seen that selective oxygen enrichment slightly increases the melt fraction in the upper sintering bed, while the time for the lower high-temperature zone to reach the bottom is significantly accelerated, and the overall visual difference between the two oxygen enrichment methods is not significant.

Figure 20 shows the comparison of the remaining radii of each case after sintering under a biochar diameter of 4.8 mm. It is evident that selective oxygen enrichment (cases 14−16, cases 20−22) significantly improves the combustion and utilization degree of biochar in the near-inlet area of the sintering bed.

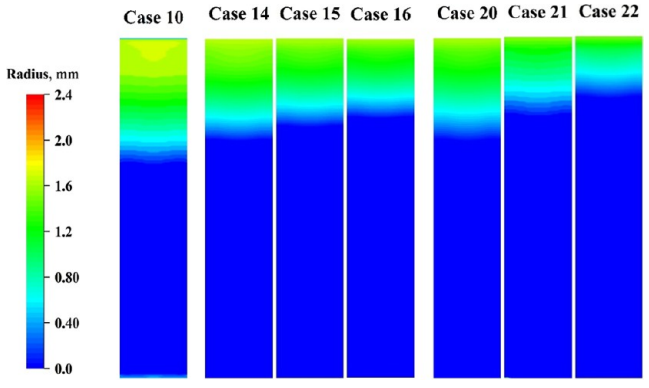

Figure 20. Residual radius contours of cases 10, 14, 15, 16, 20, 21, and 22.

Moreover, the improvement of selective oxygen coupling segregation (cases 20−22) is better than that of oxygen enrichment without segregation (cases 14−16) because at the same concentration, there is less unburned biochar on its surface layer, such as the comparison between case 16 and case 22. Oxygen enrichment can continuously penetrate the solid combustion zone, and regional oxygen enrichment can enhance the contact intensity between carbon particles and gas, accelerate the combustion of solid fuel, and release the corresponding energy, thereby improving the carbon utilization degree in the near-inlet area and the temperature state of the bed. Regarding the melt fraction in the near-inlet area, as shown in Figure 21, the selective oxygen enrichment process (cases 14, 15, and 16) is only better than case 10 in the upper bed area because it starts to melt at a shallower depth (Figure 20a: approximately 0.2 bed depth), and the range where $M_f > 0$ in the lower bed position is roughly similar. However, both the melting range ($M_f > 0$) and the yield range ($0 < M_f < 0.42$) of the selective oxygen enrichment coupled with the segregation process (cases 20, 21, and 22) are expanded compared with the non-oxygen enrichment case (case 10), and its M_f curve can completely envelope the non-oxygen enrichment situation. Obviously, the segregated oxygen enrichment concentration makes the oxygen concentration contacted by the sintering surface layer the highest, and the remaining radius cloud map (Figure 19) shows that the degree of combustion and utilization gradually improves along the surface layer. The segregated concentration corresponds to the remaining radius, which is beneficial to accelerate the combustion of the surface solid fuel and further improve the temperature state.

Figure 22 shows the combustion rates of coke and biochar at 300 and 1200 s. At 300 s, the maximum combustion rates of coke for selective oxygen enrichment (case 15) and selective oxygen enrichment coupled with segregation (case 21) are 68.64 mol/m^3 s and 81.95 mol/m^3 s, respectively, and the combustion rates of biochar are 39.25 mol/m^3 s and 48.50 mol/m^3 s, respectively. Compared with the combustion rates of coke and biochar in the case without oxygen enrichment (42.36 mol/m^3 s and 24.77 mol/m^3 s), there is a very significant increase. Among them, case 21 shows increases of 93.46% and 95.80%, respectively. The heat released from coke and biochar is sufficient, and the significantly

https://doi.org/10.1021/acsomega.6c00999
ACS Omega XXXX, XXX, XXX−XXX

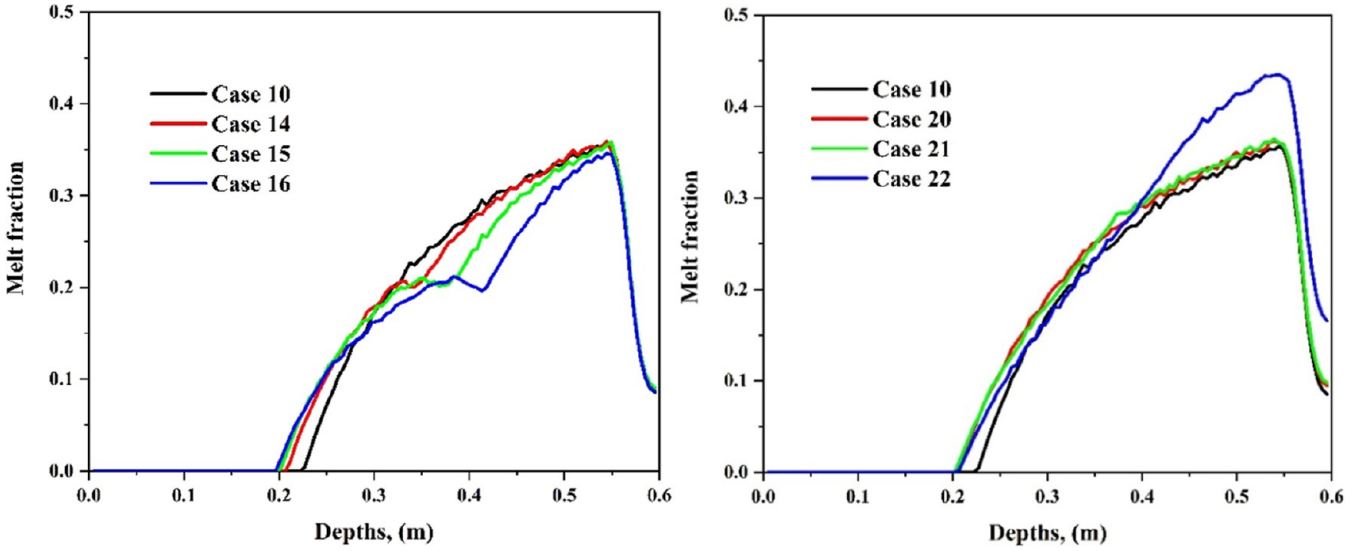

Figure 21. Melt fraction of cases 10, 14, 15, 16, 20, 21, and 22.

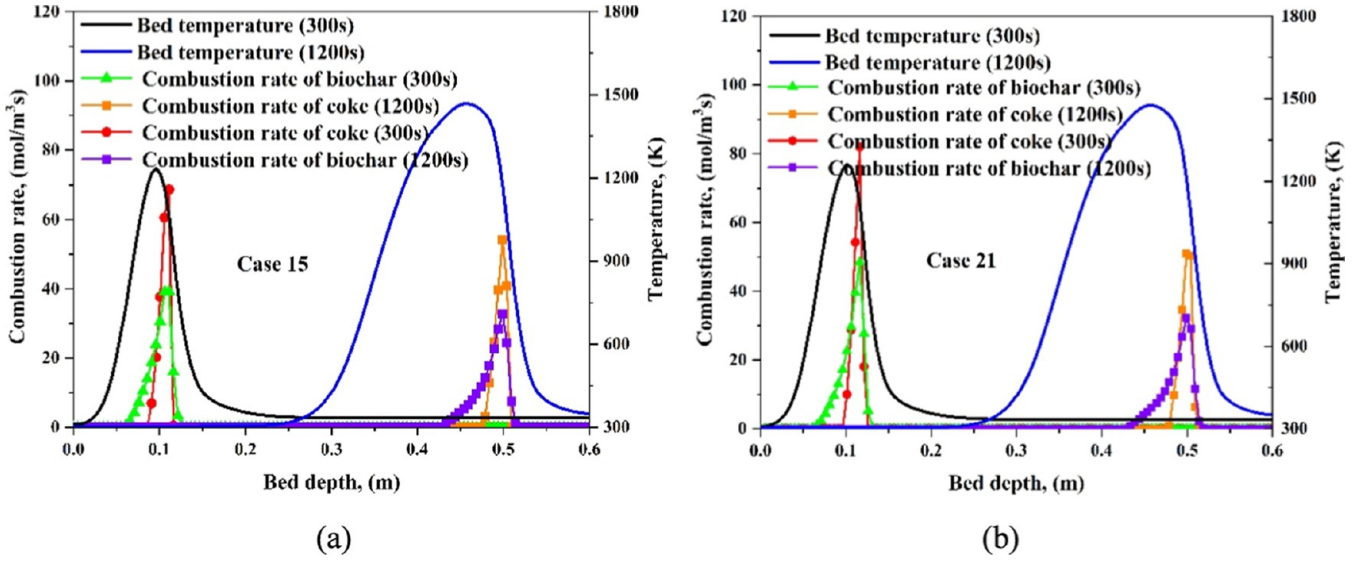

Figure 22. Combustion rates of char with cases 15 and 21 at 300 s: (a) case 15; (b) case 21.

Table 12. Average Values of Thermal Indicators for Different Cases

no	FFS (cm/min)	PT (K)	DTCZ (s)	DTMZ (s)	MQI (K·s)	CR (K/min)	ST (s)	yield (%)
case 1	2.52	1464.01	55.2	165.6	9671.34	65.40	1358	77.84
case 10	2.24	1374.93	94.4	98.8	5797.03	32.64	1530	44.22
case 21	2.51	1404.31	92.8	108	6316.07	38.12	1360	46.04
case 2X	2.53	1431.33	100.4	134.4	9557.55	55.07	1352	61.96

increased rate has greatly improved fuel utilization efficiency and the temperature state near the sintering inlet. In 1200 s, the maximum combustion rates of coke for selective oxygen enrichment (case 15) and selective oxygen enrichment coupled with segregation (case 21) were 54.24 mol/m^3 s and 50.98 mol/m^3 s, respectively, and the combustion rates of biochar were 32.87 mol/m^3 s and 32.20 mol/m^3 s, respectively. Compared with the combustion rates of coke and biochar in the non-oxygen enrichment case (52.65 mol/m^3 s and 32.77 mol/m^3 s), the changes were not significant. Among them, case 21 showed decreases of 3.17% and 1.77%, respectively. It is obvious that selective oxygen enrichment in the near-inlet area of sintering does not significantly affect the combustion rate in the lower layer of the sintering.

In summary, the use of selective oxygen enrichment in the near-inlet area of sintering can effectively improve fuel combustion and utilization efficiency and slightly increase the melting rate in the near-inlet area while maintaining the temperature and combustion rate of the middle and lower bed layers.

https://doi.org/10.1021/acsomega.6c00999
ACS Omega XXXX, XXX, XXX−XXX

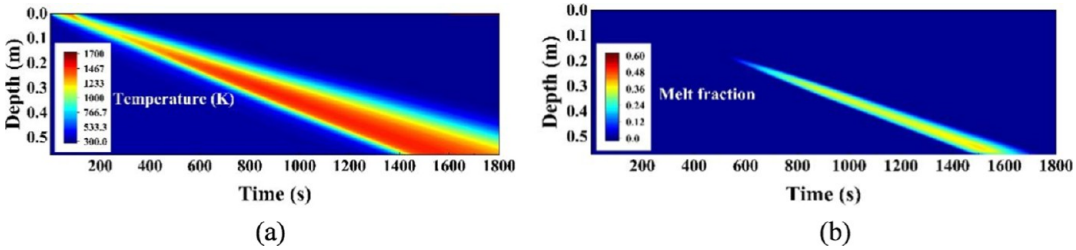

Figure 23. Two-dimensional distribution with cases 2X: (a) solid temperature; (b) melt fraction.

6. PRELIMINARY STUDIES FOR FURTHER OPTIMIZATION

Considering the strong improvement effect of selective oxygen enrichment on fuel utilization in the sintering near the inlet area, while the overall yield enhancement effect is not significant, the yield and key thermal indicators of 60% biochar sintering are still at a low level, as shown in Table 12. This section mainly considers increasing the use of selective hydrogen-rich injection combined with the aforementioned processes to enhance the thermal indicators. The selective methane injection time period is 912 s after the ignition stage, with an injection concentration of 0.58% (oxygen enrichment is 818 s after the ignition stage, and case 2X is considered as adding a selective methane injection process based on case 21).

As shown in Table 12, compared with case 10, the yield of selective hydrogen-rich injection and oxygen enrichment reached 61.96%, maintaining significant growth in key thermal indicators such as DTCZ, DTMZ, MQI, etc., approaching the method of using all coke as fuel (case 1). Figure 23 shows the two-dimensional temperature and melt distribution of case 2X. Compared with case 10 in Figure 7, the main improvement comes from the near-inlet area. These results preliminarily reflect the strong potential of using low-grade biochar combined with coarsening particle size, oxygen enrichment, and gas fuel injection processes. The authors will continue to improve in future research.

7. CONCLUSIONS

This paper addresses the issue of quality degradation when low-to-medium-grade biochar is used in the sintering process. It attempts to improve the situation by adopting process methods such as coarsening the particle size, selective oxygen enrichment, and concentration segregation along the length of the sintering machine. The results obtained are as follows:

(1) The use of the particle size coarsening method can enhance various thermal indicators of sintering when 60% biochar is substituted. The maximum yield appears at a biochar diameter of 4.0 mm, reaching 46.88%. Further increases in the biochar diameter will be affected by the expanded range of temperature reduction in the near-inlet area of the sintering bed, the decreased solid combustion rate, and reduced heat release. As a result, the yield will not increase but instead decrease. The unburned area of 4.8 mm biochar sintering accounts for nearly one-third of the bed.

(2) Taking the unburned positions on the surface layer of the sintering bed as the selective injection area and applying oxygen-enriched technology as well as oxygen-enriched coupled segregation technology to this area, it is found that both selective oxygen-enriched technologies significantly improve fuel utilization efficiency, and the oxygen-enriched technology coupled with segregation has a better improvement effect.

(3) Oxygen enrichment increases the reaction rate of biochar and coke in the solid combustion zone, greatly enhances the energy release, and strengthens the thermal curve in the near-inlet area of sintering. Compared with the situation without oxygen enrichment, the yield increased by 6.12%, mainly due to the improvement in the upper layer of the material.

In addition, the author also made preliminary attempts to use a combination of medium- and low-grade biochar coarsening particle size and selective hydrogen-rich injection and selective oxygen enrichment processes, demonstrating the potential application of multiprocess integration. In the future, the coarsened particle size and selective oxygen enrichment process can be used in combination with processes such as hydrogen-rich injection and fuel-stratified distribution more deeply. This is of great significance for further improving the sintering quality under the replacement of medium- and low-grade biochar and reducing its comprehensive use cost.

AUTHOR INFORMATION

Corresponding Authors

Jin Cai − *School of Mechanical Engineering and Automation, University of Science and Technology Liaoning, Anshan 114000, China*; orcid.org/0000-0002-9543-253X; Phone: +86-15140662469; Email: caijin_33@126.com

Xiangwei Kong − *School of Mechanical Engineering and Automation, Northeastern University, Shenyang 110819, China*; Email: shawnkongneu@163.com

Authors

Zecheng Wang − *School of Mechanical Engineering and Automation, University of Science and Technology Liaoning, Anshan 114000, China*

Mingzhu Yu − *School of Mechanical Engineering and Automation, Northeastern University, Shenyang 110819, China*

Liang Zhao − *School of Metallurgy, Northeastern University, Shenyang 110819, China*

Chunwen Yan − *School of Mechanical Engineering and Automation, University of Science and Technology Liaoning, Anshan 114000, China*

Ailing Liu − *School of Mechanical Engineering and Automation, University of Science and Technology Liaoning, Anshan 114000, China*

Hao Wu − *School of Innovation and Entrepreneurship, University of Science and Technology Liaoning, Anshan 114000, China*

Complete contact information is available at: https://pubs.acs.org/10.1021/acsomega.6c00999

https://doi.org/10.1021/acsomega.6c00999
ACS Omega XXXX, XXX, XXX−XXX

Notes

The authors declare no competing financial interest.

■ ACKNOWLEDGMENTS

The financial support for this work has been provided by the Basic Research Project of Liaoning Provincial Department of Education (LJ212510146009), and this is gratefully acknowledged.

■ REFERENCES

(1) Suopajärvi, H.; Kemppainen, A.; Haapakangas, J.; Fabritius, T. Extensive review of the opportunities to use biomass-based fuels in iron and steelmaking processes. *J. Clean. Prod.* **2017**, *148*, 709−734.
(2) Chen, W.; Yin, X.; Ma, D. A bottom-up analysis of China's iron and steel industrial energy consumption and CO2 emissions. *Appl. Energy* **2014**, *136*, 1174−1183.
(3) Cheng, Z.; Wang, J.; Wei, S.; Guo, Z.; Yang, J.; Wang, Q. Optimization of gaseous fuel injection for saving energy consumption and improving imbalance of heat distribution in iron ore sintering. *Appl. Energy* **2017**, *207*, 230−242.
(4) Cheng, Z.; Yang, J.; Zhou, L.; Liu, Y.; Guo, Z.; Wang, Q. Experimental study of commercial charcoal as alternative fuel for coke breeze in iron ore sintering process. *Energy Convers. Manag.* **2016**, *125*, 254−263.
(5) Babich, A.; Senk, D. Biomass use in the steel industry: Back to the future? *Stahl Eisen* **2013**, *133*, 57−67.
(6) Lovel, R.; Vining, K.; Dell'Amico, M. Iron ore sintering with charcoal. *Trans. Institutions Min. Metall. Sect. C Miner. Process. Extr. Metall.* **2007**, *116*, 85−92.
(7) Fan, X.; Ji, Z.; Gan, M.; Chen, X.; Yin, L.; Jiang, T. Characteristics of Prepared Coke−biochar Composite and Its Influence on Reduction of NO_x Emission in Iron Ore Sintering. *ISIJ Int.* **2015**, *55*, 521−527.
(8) Fan, X.; Ji, Z.; Gan, M.; Chen, X.; Jiang, T. Integrated assessment on the characteristics of straw-based fuels and their effects on iron ore sintering performance. *Fuel Process. Technol.* **2016**, *150*, 1−9.
(9) Gul, E.; Riva, L.; Nielsen, H. K.; Yang, H.; Zhou, H.; Yang, Q.; Skreiberg, Ø.; Wang, L.; Barbanera, M.; Zampilli, M.; Bartocci, P.; Fantozzi, F. Substitution of coke with pelletized biocarbon in the European and Chinese steel industries: An LCA analysis. *Appl. Energy* **2021**, *304*, 117644.
(10) Ji, Z.; Fan, X.; Gan, M.; Chen, X.; Li, Q.; Jiang, T. Assessment on the Application of Commercial Medium-Grade Charcoal as a Substitute for Coke Breeze in Iron Ore Sintering. *Energy Fuels* **2016**, *30*, 10448−10457.
(11) Zhao, J.; Loo, C. E.; Yuan, J.; Wang, F.; Wang, J.; Zhang, H.; Miao, H. A Fundamental Study of the Cocombustion of Coke and Charcoal during Iron Ore Sintering. *Energy Fuels* **2018**, *32*, 8743−8759.
(12) Kawaguchi, T.; Hara, M. Utilization of biomass for iron ore sintering. *ISIJ Int.* **2013**, *53*, 1599−1606.
(13) Gan, M.; Fan, X.; Ji, Z.; Jiang, T.; Chen, X.; Yu, Z.; Li, G.; Yin, L. Application of biomass fuel in iron ore sintering: Influencing mechanism and emission reduction. *Ironmak. Steelmak.* **2015**, *42*, 27−33.
(14) Cheng, Z.; Yang, J.; Zhou, L.; Liu, Y.; Wang, Q. Characteristics of charcoal combustion and its effects on iron-ore sintering performance. *Appl. Energy* **2016**, *161*, 364−374.
(15) Cheng, Z.; Wei, S.; Guo, Z.; Yang, J.; Wang, Q. Improvement of heat pattern and sinter strength at high charcoal proportion by applying ultra-lean gaseous fuel injection in iron ore sintering process. *J. Clean. Prod.* **2017**, *161*, 1374−1384.
(16) Kang, H.; Choi, S.; Yang, W.; Cho, B. Influence of oxygen supply in an iron ore sintering process. *ISIJ Int.* **2011**, *51*, 1065−1071.
(17) Kang, H.; Choi, S.; Yang, W.; Cho, B. Effective utilization of operating condition in production of sintered ore. *Proc. Inst. Mech. Eng. Part A J. Power Energy* **2012**, *226*, 37−48.
(18) Iwami, Y.; Yamamoto, T.; Higuchi, T.; Nushiro, K.; Sato, M.; Oyama, N. Effect of oxygen enrichment on sintering with combined usage of coke breeze and gaseous fuel. *ISIJ Int.* **2013**, *53*, 1633−1641.
(19) Cheng, Z.; Guo, Z.; Fu, P.; Yang, J.; Wang, Q. New insights into the effects of methane and oxygen on heat/mass transfer in reactive porous media. *Int. Commun. Heat Mass Transfer* **2021**, *129*, 105652.
(20) Ni, W.; Jiang, L.; Zhu, X.; Yi, X.; Li, H.; Shao, L.; Meng, F.; Zou, Z. Numerical simulation of iron ore sintering process with coke oven gas injection and oxygen enrichment. *Int. J. Chem. React. Eng.* **2022**, *20*, 1035−1051.
(21) de Castro, J. A. Model predictions for new iron ore sintering process technology based on biomass and gaseous fuels. *Adv. Mater. Res.* **2014**, *918*, 136−144.
(22) de Castro, J. A.; de Oliveira, E. M.; de Campos, M. F.; Takano, C.; Yagi, J.-i. Analyzing cleaner alternatives of solid and gaseous fuels for iron ore sintering in compacts machines. *J. Clean. Prod.* **2018**, *198*, 654−661.
(23) Cai, J.; Kong, X.; Cheng, L.; Yu, M. Mathematical modeling and characteristics evaluation of coke replacing with commercial biochar in iron ore sintering process. *Fuel* **2024**, *377*, 132820.
(24) Cai, J.; Kong, X.; Cheng, L.; Yu, M.; Qi, H.; Zhang, J. Numerical simulation of the Co-combustion of coke and biochar coupled with methane injection in iron ore sintering processes. *Int. J. Hydrogen Energy* **2024**, *82*, 1114−1130.
(25) Wang, G.; Wen, Z.; Lou, G.; Dou, R.; Li, X.; Liu, X.; Su, F. Mathematical modeling of and parametric studies on flue gas recirculation iron ore sintering. *Appl. Therm. Eng.* **2016**, *102*, 648.
(26) Pahlevaninezhad, M.; Davazdah Emami, M.; Panjepour, M. The effects of kinetic parameters on combustion characteristics in a sintering bed. *Energy* **2014**, *73*, 160.
(27) Ergun *Chemical Engineering Progress*, 1952.
(28) Collazo, J.; Porteiro, J.; Patiño, D.; Granada, E. Numerical modeling of the combustion of densified wood under fixed-bed conditions. *Fuel* **2012**, *93*, 149−159.
(29) Wang, G.; Wen, Z.; Lou, G.; Dou, R.; Li, X.; Liu, X.; Su, F. Mathematical modeling and combustion characteristic evaluation of a flue gas recirculation iron ore sintering process. *Int. J. Heat Mass Transfer* **2016**, *97*, 964.
(30) Chan, W. C. R.; Kelbon, M.; Krieger, B. B. Modelling and experimental verification of physical and chemical processes during pyrolysis of a large biomass particle. *Fuel* **1985**, *64*, 1505−1513.
(31) Thurner, F.; Mann, U. Kinetic Investigation of Wood Pyrolysis. *Ind. Eng. Chem. Process Des. Dev.* **1981**, *20*, 482−488.
(32) Wagenaar, B. M.; Prins, W.; van Swaaij, W. P. M. Flash pyrolysis kinetics of pine wood. *Fuel Process. Technol.* **1993**, *36*, 291−298.
(33) Yang, Y. B.; Goh, Y. R.; Zakaria, R.; Nasserzadeh, V.; Swithenbank, J. Mathematical modelling of MSW incineration on a travelling bed. *Waste Manag* **2002**, *22*, 369−380.
(34) Donghoon, S.; Sangmin, C. The combustion of simulated waste particles in a fixed bed. *Combust. Flame* **2000**, *121*, 167−180.
(35) Miljković, B.; Pešenjanski, I.; Vićević, M. Mathematical modelling of straw combustion in a moving bed combustor: A two dimensional approach. *Fuel* **2013**, *104*, 351−364.
(36) Macak, J.; Malecha, J. Mathematical Model for the Gasification of Coal under Pressure. *Ind. Eng. Chem. Process Des. Dev.* **1978**, *17*, 92−98.
(37) Thunman, H.; Leckner, B.; Niklasson, F.; Johnsson, F. Combustion of wood particles - A particle model for Eulerian calculations. *Combust. Flame* **2002**, *129*, 30−46.
(38) Zhang, S.; Wen, Z.; Wang, G.; Dou, R.; Liu, X.; Li, X. The effects of operational parameters on flue gas recirculation iron ore sintering process: sensitivity analysis based on numerical simulation and industrial onsite experimental validation. *Ironmak. Steelmak.* **2020**, *47*, 368−380.
(39) Johansson, R.; Thunman, H.; Leckner, B. Influence of intraparticle gradients in modeling of fixed bed combustion. *Combust. Flame* **2007**, *149*, 49−62.
(40) Zhou, H.; Zhao, J. P.; Loo, C. E.; Ellis, B. G.; Cen, K. F. Numerical modeling of the iron ore sintering process. *ISIJ Int.* **2012**, *52*, 1550.
(41) Huang, X. X.; Fan, X. H.; Chen, X. L.; Zhao, X. Z.; Gan, M. Optimisation model of fuel distribution in materials bed of iron ore sintering process. *Ironmak. Steelmak.* **2019**, *46*, 649.

https://doi.org/10.1021/acsomega.6c00999
ACS Omega XXXX, XXX, XXX−XXX

(42) Seenivasan, R.; Acharyulu, A. V. B.; Sabariraj, V.; Arvind, J.; Rameshwar, S.; Balachandran, G. Modelling the effect of sinter machine speed on bed temperature and coke combustion characteristics in iron ore sintering process. *Ironmak. Steelmak.* **2021**, *48*, 637−648.
(43) Irabien, A.; Viguri, J. R.; Ortiz, I. Thermal Dehydration of Calcium Hydroxide. 1. Kinetic Model and Parameters. *Ind. Eng. Chem. Res.* **1990**, *29*, 1599−1606.
(44) Zhang, X.-H.; Feng, P.; Xu, J.-R.; Feng, L.-B.; Qing, S. Numerical research on combining flue gas recirculation sintering and fuel layered distribution sintering in the iron ore sintering process. *Energy* **2020**, *192*, 116660.
(45) Hara, Y.; Tsuchiya, M.; Kondo, S. Intraparticle Temperature of Iron-Oxide Pellet during the Reduction. *Tetsu-to-Hagane* **1974**, *60*, 1261−1270.
(46) Omori, Y. *Blast Furnace Phenomena and Modelling*; Elsevier: London, 1987.10.1007/978-94-009-3431-3.
(47) Zhang, B.; Zhou, J.; Li, M. Prediction of sinter yield and strength in iron ore sintering process by numerical simulation. *Appl. Therm. Eng.* **2018**, *131*, 70.
(48) Zhao, J. Numerical simulation and experimental verification of iron ore sintering process; Ph.D.Thesis; Hangzhou: Zhejiang University, 2012.
(49) De Soete, G. G. Overall reaction rates of NO and N2 formation from fuel nitrogen. *Symp. Combust.* **1975**, *15*, 1093−1102.
(50) Hill, S. C.; Douglas Smoot, L. Modeling of nitrogen oxides formation and destruction in combustion systems. *Prog. Energy Combust. Sci.* **2000**, *26*, 417−458.
(51) Lockwood, F. S.; Romo Millares, C. A. Assessment of kinetic and mixing-controlled models for the prediction of fuel-no emissions in p.f. burners. *Combust. Sci. Technol.* **1994**, *102*, 57−80.
(52) Zeng, L.; Li, Z.; Zhao, G.; Shen, S.; Zhang, F. Numerical simulation of combustion characteristics and NOx emissions in a 300 MWe utility boiler with different outer secondary-air vane angles. *Energy Fuels* **2010**, *24*, 5349−5358.
(53) Le Bris, T.; Cadavid, F.; Caillat, S.; Pietrzyk, S.; Blondin, J.; Baudoin, B. Coal combustion modelling of large power plant, for NOx abatement. *Fuel* **2007**, *86*, 2213−2220.
(54) Karlström, O.; Brink, A.; Hupa, M. Biomass char nitrogen oxidation - Single particle model. *Energy Fuels* **2013**, *27*, 1410−1418.
(55) Zhou, H.; Zhou, M.; Liu, Z.; Cheng, M.; Chen, J. Modeling NOx emission of coke combustion in iron ore sintering process and its experimental validation. *Fuel* **2016**, *179*, 322.
(56) Ni, W.; Li, H.; Zhang, Y.; Zou, Z. Effects of fuel type and operation parameters on combustion and NO x emission of the iron ore sintering process. *Energies* **2019**, *12*, 213.
(57) Han, J.; Lou, G.; Zhang, S.; Wen, Z.; Liu, X.; Liu, J. The effects of coke parameters and circulating flue gas characteristics on NOx emission during flue gas recirculation sintering process. *Energies* **2019**, *12*, 3828.
(58) Lockwood, F. C.; Romo-Millares, C. A. Mathematical modelling of fuel-NO emissions from PF burners. *J. Inst. Energy* **1992**, *65*, 144−152.
(59) Schaffel, N.; Mancini, M.; Szlęk, A.; Weber, R. Mathematical modeling of MILD combustion of pulverized coal. *Combust. Flame* **2009**, *156*, 1771−1784.
(60) De Soete, G. G.; Croiset, E.; Richard, J. R. Heterogeneous formation of nitrous oxide from char-bound nitrogen. *Combust. Flame* **1999**, *117*, 140−154.
(61) Jensen, A.; Johnsson, J. E.; Andries, J.; Laughlin, K.; Read, G.; Mayer, M.; Baumann, H.; Bonn, B. Formation and reduction of NOx in pressurized fluidized bed combustion of coal. *Fuel* **1995**, *74*, 1555−1569.
(62) Zhang, J.; Sun, S.; Hu, X.; Sun, R.; Qin, Y. Modeling no - Char reaction at high temperature. *Energy Fuels* **2009**, *23*, 2376−2382.
(63) Díez, L. I.; Cortés, C.; Pallarés, J. Numerical investigation of NOx emissions from a tangentially-fired utility boiler under conventional and overfire air operation. *Fuel* **2008**, *87*, 1259−1269.
(64) Ni, W. Simulation and Optimization of Flue Gas Recirculation for Iron Ore Sintering with Oxygen Enrichment and Coke Oven Gas Injection; Ph.D.Thesis; Northeastern University, 2019.
(65) Wang, G. Numerical Simulation and Application of Heat and Mass Transfer Process in Waste Gas Circulation Sintering; Ph.D.Thesis; University of Science and Technology Beijing, 2017.
(66) Zhang, B.; Zhou, Z.; Li, M. Heat and mass transfer analysis of double-layer carbon sintering process. *Journal of Chemical Engineering* **2017**, *68*, 1811−1822.
(67) Yang, W.; Ryu, C.; Choi, S.; Choi, E.; Lee, D.; Huh, W. Modeling of combustion and heat transfer in an iron ore sintering bed with considerations of multiple solid phases. *ISIJ Int.* **2004**, *44*, 492−499.
(68) Yang, W.; Choi, S.; Choi, E. S.; Ri, D. W.; Kim, S. Combustion characteristics in an iron ore sintering bed-evaluation of fuel substitution. *Combust. Flame* **2006**, *145*, 447−463.
(69) Shrestha, S.; Xu, J.; Yu, A.; Zhou, Z. Numerical simulation of fuel layered distribution iron ore sintering technology. *Ironmak. Steelmak.* **2022**, *49*, 83−100.
(70) Pahlevaninezhad, M.; Emami, M. D.; Panjepour, M. Identifying major zones of an iron ore sintering bed. *Appl. Math. Model.* **2016**, *40*, 8475−8492.
(71) Ni, W.; Li, H.; Shao, L.; Zou, Z. Numerical simulation on influence of coke oven gas injection on iron ore sintering. *ISIJ Int.* **2020**, *60*, 662−673.
(72) Gan, M.; Fan, X.; Chen, X.; Ji, Z.; Lv, W.; Wang, Y.; Yu, Z.; Jiang, T. Reduction of pollutant emission in iron ore sintering process by applying biomass fuels. *ISIJ Int.* **2012**, *52*, 1574−1578.
(73) Gan, M.; Ji, Z.; Fan, X.; Zhao, Y.; Chen, X.; Fan, Y. Insight into the high proportion application of biomass fuel in iron ore sintering through CO-containing flue gas recirculation. *J. Clean. Prod.* **2019**, *232*, 1335−1347.
(74) Gan, M.; Fan, X.; Ji, Z.; Chen, X.; Jiang, T.; Yu, Z. Effect of distribution of biomass fuel in granules on iron ore sintering and NOx emission. *Ironmak. Steelmak.* **2014**, *41*, 430−434.
(75) Wijayanta, A. T.; Alam, M. S.; Nakaso, K.; Fukai, J.; Kunitomo, K.; Shimizu, M. Numerical study on pulverized biochar injection in blast furnace. *ISIJ Int.* **2014**, *54*, 1521−1529.
(76) Blaskett, R. No Title. In *Sinter. Symp.* 1960; pp 61−70.
(77) Cheng, Z.; Fu, P.; Guo, Z.; Yang, J.; Wang, Q. CFD prediction of heat/mass transfer in multi-layer sintering process assisted with gaseous fuel injection. *Int. Commun. Heat Mass Transfer* **2021**, *128*, 105654.

https://doi.org/10.1021/acsomega.6c00999
ACS Omega XXXX, XXX, XXX−XXX